

# Incompressible multiphase flow and encapsulation simulations using the moment-of-fluid method

Guibo Li<sup>1</sup>, Yongsheng Lian<sup>1</sup>, Yisen Guo<sup>1</sup>, Matthew Jemison<sup>2</sup>, Mark Sussman<sup>2,\*†</sup>,  
Trevor Helms<sup>2</sup> and Marco Arienti<sup>3</sup>

<sup>1</sup>Mechanical Engineering Department, University of Louisville, Louisville, KY, USA

<sup>2</sup>Department of Mathematics, Florida State University, Tallahassee, FL, USA

<sup>3</sup>Sandia National Laboratories, Livermore, CA, USA

## SUMMARY

A moment-of-fluid method is presented for computing solutions to incompressible multiphase flows in which the number of materials can be greater than two. In this work, the multimaterial moment-of-fluid interface representation technique is applied to simulating surface tension effects at points where three materials meet. The advection terms are solved using a directionally split cell integrated semi-Lagrangian algorithm, and the projection method is used to evaluate the pressure gradient force term. The underlying computational grid is a dynamic block-structured adaptive grid. The new method is applied to multiphase problems illustrating contact-line dynamics, triple junctions, and encapsulation in order to demonstrate its capabilities. Examples are given in two-dimensional, three-dimensional axisymmetric ( $R$ - $Z$ ), and three-dimensional ( $X$ - $Y$ - $Z$ ) coordinate systems. Copyright © 2015 John Wiley & Sons, Ltd.

Received 28 June 2014; Revised 14 May 2015; Accepted 31 May 2015

KEY WORDS: multiphase flow; moment-of-fluid method; interface

## 1. INTRODUCTION

Multiphase flow plays an important role in many technical applications including ink-jet printing, spray cooling, icing, combustion, and agricultural irrigation. The instability of the interface, mass and heat transfer across the interface, and phase change make multiphase flow problems challenging. Theoretical studies of multiphase flows are mainly based on linear theories [1, 2] but most phenomena in multiphase flows display nonlinear feedback mechanisms. Modern experimental studies employ high-speed cameras, pulsed shadowgraph, and holograph techniques [3–5] in order to understand the complex processes in multiphase flows; nonetheless, it is still very difficult to capture the detailed flow fields.

Computational fluid dynamics (CFD) has the potential to increase ones' understanding of multiphase flow phenomena by allowing one to investigate flow fields deeply embedded within materials, study the effect of random fluctuations, and precisely control initial and boundary conditions. Quantities such as interface surface area, streamlines, stress fields, and vorticity are easily extracted from CFD simulations. Three major challenges exist for the accurate and efficient computation of multiphase flows. First, the density and viscosity ratios between different phases can be high, and it is difficult to accurately calculate the flux during the momentum advection [6, 7]. Second, surface tension takes effect only at the interface between different phases, and this singularity may cause problems when solving the Navier–Stokes equations [8, 9]. Third, the drastic change of interface

---

\*Correspondence to: Mark Sussman, Department of Mathematics, Florida State University, Tallahassee, FL, USA.

†E-mail: sussman@math.fsu.edu

topology and disparity in length scales make interface capturing and interface advection challenging [10, 11].

Among the different interface-capturing methods, the volume-of-fluid (VOF) method [8, 12, 13], the level set method [14–18], and their derivatives are widely used.

The VOF method tracks the volume fraction function within each computational grid cell. The interface is reconstructed and advected based on the volume fraction function information. The benefit of VOF methods is that there have been devised either directionally split advection algorithms [19–22] or unsplit advection algorithms [23–25], which have excellent volume preservation properties.

The level set method uses a smooth distance function to implicitly represent the interface. On the one hand, the level set method is amenable to computing flows with surface tension effects because the distance function is smooth across the interface; on the other hand, volume conservation for the level set method is not guaranteed, even if the level set advection equation is discretized in conservation form. The coupled level set and VOF (CLSVOF) method [10, 26–29] has also been developed. Even though the specific implementations of CLSVOF methods vary, the overriding theme of CLSVOF methods is that they maintain the advantages of both the level set method and the VOF method in simultaneously conserving volume and accurately capturing the interface [26, 29].

Recently, the moment-of-fluid (MOF) method [21, 25, 30–35] has been developed. In addition to the volume fraction function used in the VOF method, the MOF method considers the material centroid information in the interface reconstruction process and can be considered a generalization of the VOF method. The MOF interface reconstruction is completely local because of the introduction of centroid information. This feature enables the MOF method to capture corners and sheets significantly better than the VOF method for passively advected flows. Results of benchmark tests comparing MOF with VOF and CLSVOF are reported in [21, 36, 37]. A further advantage of the MOF representation is that the added centroid information enables the MOF method to straightforwardly reconstruct any number of materials, that is, two or more, in a given cell, conserving the volume of each material [25, 31].

We remark that there have previously been developed the following VOF triple junction reconstruction algorithms: the ‘onion skin’ approach in which the materials do not intersect [38], the material order-independent weighted Voronoi diagram (also known as a power diagram) approach for 2D reconstruction of triple points applied to static configurations [39], an optimization method for the localization of the triple points applied to 2D passive transport problems [40], and an improved material order-independent weighted Voronoi diagram approach in which a novel optimization procedure was developed for determining interface(s) normals [41].

We have taken the ‘nested dissection’ MOF approach; if a computational cell contains  $M$  materials, then there will be  $M - 1$  linear cuts in the cell, some cuts potentially intersecting previous cuts. The MOF algorithm can reconstruct interface configurations where three materials meet at a single point, albeit one of the angles separating two of the materials must be  $90^\circ$ .

In this paper, we describe a novel method in which we use the MOF multimaterial reconstruction algorithm in order to simulate incompressible multiphase flow in two (2D) or three dimensions (3D) in which (i) two fluids with disparate material properties can meet at a third rigid material (contact-line dynamics) and (ii) three fluids with disparate material properties meet at a triple junction. As in [35], we maintain and update the velocity at both cell centers and face centers. The velocity is interpolated from cell centers to face centers using mass weighting where the MOF reconstruction determines the weights. Pressure is interpolated from cell centers to face centers using the condition of constant contact, where again the weights depend on the MOF reconstructed interface.

In what follows, we describe our incompressible multiphase MOF method, and we describe the algorithm that we have developed for the simulation of contact-line dynamics and triple-point dynamics. Example simulations are given with validations through grid refinement studies and comparisons with experiments, and finally, conclusions are drawn.

## 2. GOVERNING EQUATIONS

The governing equations for incompressible, immiscible, multiphase flows are

$$\nabla \cdot \mathbf{u} = 0 \quad (1)$$

$$\frac{\partial \phi_m}{\partial t} + \mathbf{u} \cdot \nabla \phi_m = 0, \quad m = 1, \dots, M \quad (2)$$

$$\frac{\partial \mathbf{u}}{\partial t} + \mathbf{u} \cdot \nabla \mathbf{u} = -\frac{\nabla p_m}{\rho_m} + \frac{\nabla \cdot (2\mu_m D)}{\rho_m} + \mathbf{g} \quad \text{if } \phi_m(\mathbf{x}, t) > 0 \quad (3)$$

where  $\phi_m$  is a level set function for material  $m$  and satisfies

$$\phi_m(\mathbf{x}, t) = \begin{cases} > 0 & \mathbf{x} \in \text{material } m \\ \leq 0 & \text{otherwise} \end{cases}$$

$\mathbf{u} = (u, v, w)$  is the velocity vector,  $t$  is the time,  $p_m$  is the pressure for material  $m$ ,  $\mathbf{g}$  is the gravitational acceleration vector,  $D$  is the rate of deformation tensor,

$$D = \frac{\nabla \mathbf{u} + (\nabla \mathbf{u})^T}{2}$$

and  $\mu_m$  and  $\rho_m$  are the viscosity and density, respectively, for material  $m$ .

At material interfaces, if there is no mass transfer, the velocity for all materials is the same. For two-phase flow problems ( $M = 2$ ), at a material interface that separates material  $m_1$  from  $m_2$  (i.e.,  $\phi_{m_1}(\mathbf{x}, t) = \phi_{m_2}(\mathbf{x}, t) = 0$ ), the stress will have the following jump condition owing to the effect of the surface tension force:

$$((-p_{m_1} I + 2\mu_{m_1} D) - (-p_{m_2} I + 2\mu_{m_2} D)) \cdot \mathbf{n}_{m_1} = \sigma_{m_1, m_2} \kappa_{m_1} \mathbf{n}_{m_1}$$

where  $\sigma_{m_1, m_2}$  is the surface tension coefficient; the normal that points from material  $m_2$  into  $m_1$  is

$$\mathbf{n}_{m_1} = \frac{\nabla \phi_{m_1}}{|\nabla \phi_{m_1}|}$$

and the curvature is

$$\kappa_{m_1} = \nabla \cdot \frac{\nabla \phi_{m_1}}{|\nabla \phi_{m_1}|}$$

A one-fluid formulation of (3) can be written as follows [42]:

$$\frac{\partial \rho \mathbf{u}}{\partial t} + \nabla \cdot (\rho \mathbf{u} \otimes \mathbf{u}) = -\nabla p + \nabla \cdot (2\mu D) + \rho \mathbf{g} - \sum_{m=1}^M \gamma_m \kappa_m \nabla H(\phi_m) \quad (4)$$

where  $H(\phi)$  is the Heaviside function defined as

$$H(\phi) = \begin{cases} 1 & \phi \geq 0 \\ 0 & \text{otherwise} \end{cases} \quad (5)$$

the combined density  $\rho$  is

$$\rho = \sum_{m=1}^M \rho_m H(\phi_m)$$

the combined viscosity,  $\mu$ , is

$$\mu = \sum_{m=1}^M \mu_m H(\phi_m)$$

and (three-material case)

$$\gamma_1 = \frac{\sigma_{12} + \sigma_{13} - \sigma_{23}}{2} \quad (6)$$

$$\gamma_2 = \frac{\sigma_{12} + \sigma_{23} - \sigma_{13}}{2} \quad (7)$$

$$\gamma_3 = \frac{\sigma_{13} + \sigma_{23} - \sigma_{12}}{2} \quad (8)$$

### 3. NUMERICAL METHOD

We describe our numerical method for 2D problems, but the method is straightforwardly generalizable to 3D.

#### 3.1. Overview of the method

The numerical method, which is based on an approximate projection method [21], is given in the following list of steps. The spatial discretization details for each step are explained in the ensuing sections.

- At the beginning of the time step  $t = t^n$  and in each computational cell,

$$\Omega_{i,j} = \{x : x_i - \Delta x/2 < x < x_i + \Delta x/2, y_j - \Delta y/2 < y < y_j + \Delta y/2\},$$

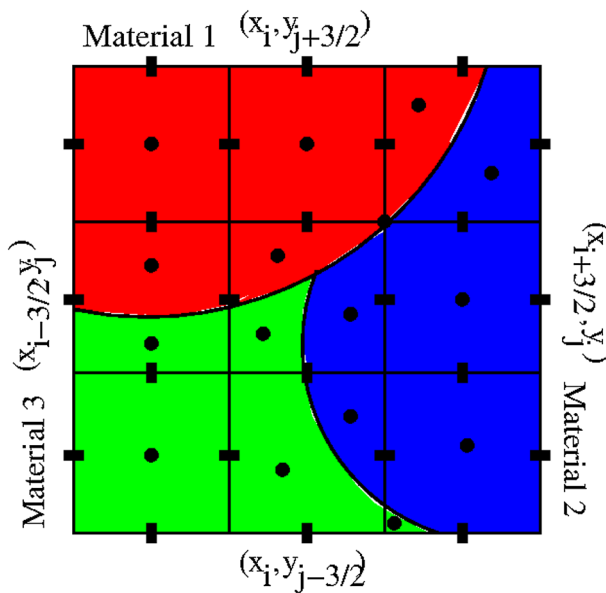


Figure 1. The volume fractions  $F_m$ , centroids  $x_m$  (filled-in circles), and cell-centered velocity  $\mathbf{u}$  are cell-averaged quantities, and the face-centered velocity (filled-in rectangles)  $u^{MAC}$  and  $v^{MAC}$  are face-averaged quantities. There are three materials illustrated in this figure. The center coordinate of the illustrated  $3 \times 3$  block of cells is  $(x_i, y_j)$ .

the following variables are given: mass-weighted average of velocity ( $\bar{\mathbf{u}}_{i,j}^n$ ), discretely divergence-free velocity on MAC grid (MAC=Marker And Cell, also known as face centered grid),

$$\frac{\bar{u}_{i+1/2,j}^{MAC,n} - \bar{u}_{i-1/2,j}^{MAC,n}}{\Delta x} + \frac{\bar{v}_{i,j+1/2}^{MAC,n} - \bar{v}_{i,j-1/2}^{MAC,n}}{\Delta y} = 0$$

volume fraction,  $F_{m,i,j}^n$ , and centroid,  $\mathbf{x}_{m,i,j}^n$ , for each material  $m$ . Figure 1 illustrates our discretization.

2. *Advection*: Referring to (4) and (2), the directionally split cell integrated semi-Lagrangian (CISL) method is used to solve the following equations:

$$(\rho\mathbf{u})_t + \nabla \cdot (\rho\mathbf{u} \otimes \mathbf{u}) = 0 \quad (9)$$

$$(F_m)_t + \nabla \cdot (\mathbf{u} F_m) = 0 \quad (10)$$

The details of CISL advection are given in Section 3.2.

3. *Distance functions*: Distance functions,  $\phi_{m,i,j}^{n+1}$ , are derived from the non-tessellating MOF reconstructed interface for each material  $m = 1, \dots, M$ . The distance functions are used to approximate interface curvature. See Section 3.3.
4. *Viscosity, gravity, surface tension*: Referring to (4),

$$\mathbf{V} = \mathbf{u}^{advect} + \Delta t \frac{1}{\rho} \left( \nabla \cdot (2\mu D) + \rho\mathbf{g} - \sum_{m=1}^M \gamma_m \kappa_m \nabla H(\phi_m) \right) \quad (11)$$

See Sections 3.4 and 3.5.

5. *Approximate projection*: A variable density approximate projection algorithm is used to discretize the pressure gradient force,

$$\mathbf{u}^{n+1} = \mathbf{V} - \Delta t \frac{\nabla p}{\rho}$$

where  $p$  solves

$$\nabla \cdot \frac{\nabla p}{\rho} = \frac{1}{\Delta t} \nabla \cdot \mathbf{V}$$

See Section 3.6

6. The block-structured adaptive grid is regenerated depending on the new locations of material interfaces, and then the algorithm returns back to step 2.

### 3.2. Directionally split cell integrated semi-Lagrangian multiphase advection

The CISL algorithm has three parts: (i) interface reconstruction, (ii) momentum reconstruction, and (ii) mapping of reconstructed solution into computational cells from a given cells' preimage.

**3.2.1. Moment-of-fluid interface reconstruction.** The MOF method [21, 30–33] is used to represent material interfaces. For a computational cell  $\Omega_{i,j}$ , the volume fraction (zeroth-order moment) and centroid (first-order moment) are

$$F_m = \frac{1}{|\Omega_{i,j}|} \int_{\Omega_{i,j}} H(\phi_m(\mathbf{x})) d\mathbf{x}$$

$$\mathbf{x}_m = \frac{\int_{\Omega_{i,j}} H(\phi_m(\mathbf{x})) \mathbf{x} d\mathbf{x}}{\int_{\Omega_{i,j}} H(\phi_m(\mathbf{x})) d\mathbf{x}}$$

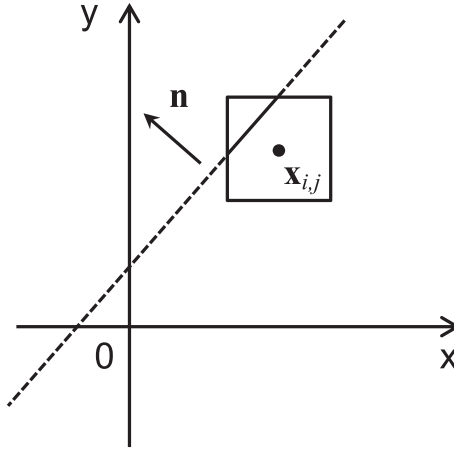


Figure 2. The gas–liquid interface is represented by a straight line in two dimensions. The square represents a computational cell, and  $\mathbf{x}_{i,j}$  is the coordinate of the cell center.

When there are two materials in a cell, the material interface is reconstructed as a plane in 3D and a line in 2D. This interface representation is called the piecewise linear interface calculation. Take a 2D case for example, an interface  $\Gamma$  in cell  $\Omega_{i,j}$  is represented by a straight line as shown in Figure 2 using the following vector form equation:

$$\Gamma = \Omega_{i,j} \cap \{\mathbf{x} | \mathbf{n} \cdot (\mathbf{x} - \mathbf{x}_{i,j}) + b = 0\} \quad (12)$$

where  $\mathbf{n}$  is the interface unit normal vector,  $\mathbf{x}_{i,j}$  is the cell center of  $\Omega_{i,j}$ , and  $b$  is the distance from  $\mathbf{x}_{i,j}$  to the interface. Thus, the interface can be constructed when the normal vector  $\mathbf{n}$  and distance  $b$  are known.

In order to find the slope and intercept of the reconstructed plane (line in 2D), we use the reference volume fraction,  $F_{ref}$ , and the reference centroid,  $\mathbf{x}_{ref}^c$ . The reference volume fraction and centroid correspond to the real interface, which is not necessarily a straight line. The slope  $\mathbf{n}$  and intercept  $b$  are selected so that the actual volume fraction function  $F_{act} = F_{act}(\mathbf{n}, b)$  is equal to  $F_{ref}$  and the actual centroid  $\mathbf{x}_{act}^c(\mathbf{n}, b)$  is as close as possible to  $\mathbf{x}_{ref}^c$ . In other words,  $\mathbf{n}$  and  $b$  are chosen in order to minimize  $E_{MOF}$  (13) subject to the volume fraction constraint given in (14):

$$E_{MOF} = \|\mathbf{x}_{ref}^c - \mathbf{x}_{act}^c(\mathbf{n}, b)\|_2 \quad (13)$$

$$|F_{ref} - F_{act}(\mathbf{n}, b)| = 0 \quad (14)$$

An example of a real interface and the corresponding reconstructed interface is illustrated in Figure 3. The curved solid line in the left figure represents the true interface, and the dashed line in the right figure is the reconstructed interface. In Figure 3,  $\mathbf{x}_{ref}^c$  is the centroid of the reference interface whose volume fraction  $F_{ref}$  is the blue area under the solid curved line, and  $\mathbf{x}_{act}^c$  is the computed centroid of the actual reconstructed interface whose volume fraction  $F_{act}$  is the blue area under the dashed straight line.

Because the normal vector  $\mathbf{n}$  can be parametrized using

$$\mathbf{n} = \begin{pmatrix} \sin(\Phi) \cos(\Theta) \\ \sin(\Phi) \sin(\Theta) \\ \cos(\Phi) \end{pmatrix} \quad (15)$$

$E_{MOF}$  becomes a function of angles  $\Phi$  and  $\Theta$ . Therefore, we need to find  $(\Phi^*, \Theta^*)$  such that

$$E_{MOF}(\Phi^*, \Theta^*) = \|f(\Phi^*, \Theta^*)\|_2 = \min \|f(\Phi, \Theta)\|_2 \quad (16)$$

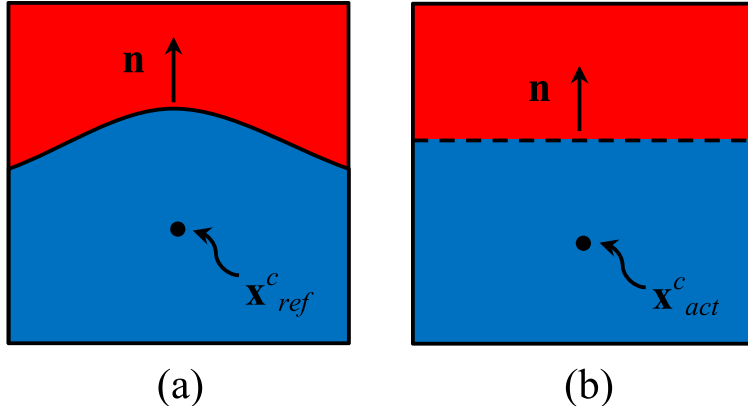


Figure 3. Moment-of-fluid interface reconstruction. (a) The solid curved line represents the real interface, and (b) the dashed straight line is the reconstructed interface.

where

$$f(\Phi, \Theta) = x_{ref}^c - x_{act}^c(\Phi, \Theta)$$

The problem becomes a nonlinear least square problem for  $(\Phi, \Theta)$ . Equation (16) is solved numerically by the Gauss-Newton algorithm, and the detailed step-by-step procedure is as follows:

0. Choose initial angles  $(\Phi_0, \Theta_0)$  and set tolerance  $tol = 10^{-8} \Delta x$  with  $\Delta x$  as the grid size. while not converged set  $k = 1$ 
    1. Find  $b_k(\Phi_k, \Theta_k)$  such that equation (14) holds.
    2. Find centroid  $x_k^c(b_k, \Phi_k, \Theta_k)$ .
    3. Find Jacobian matrix  $J_k$  of  $f$  evaluated at  $(\Phi_k, \Theta_k)$  and  $f_k = f(\Phi_k, \Theta_k)$ .
    4. Stop if one of the following three conditions is fulfilled:
      - $\|J_k^T \cdot f_k\| < tol \cdot 10^{-2} \Delta x$
      - $\|f_k\| < tol$
      - $k = 11$
    5. Solve the linear least squares problem,

$$s_k = \operatorname{argmin}_s |J_k s + f_k|_2$$

using the normal equations:  $J_k^T J_k s_k = J_k^T f_k$ .

6. Update the angles:  $(\Phi_{k+1}, \Theta_{k+1}) = (\Phi_k, \Theta_k) + s_k$ .
  7.  $k := k + 1$  and go back to step 1.

The detailed process for the minimization of equation (13) can be found in [21]. Unlike the VOF method, the MOF interface reconstruction method only uses information from the computational cell under consideration. This property makes the MOF method more suitable for deforming boundary problems with sharp corners, with slender filaments, or with greater than two materials. Also, the MOF reconstruction algorithm makes itself more suitable for block-structured dynamic adaptive mesh refinement (AMR) because conditions at coarse-grid/fine-grid interface can be interpolated from the coarse grid using a stencil that does not depend circularly on the neighboring fine grid.

When there are greater than two materials in cell ( $M > 2$ )  $\Omega_{i,j}$ , the following extension of the two-material MOF reconstruction procedure determines  $M$  polygonal regions,  $\Omega_m$ , that tessellate  $\Omega_{i,j}$  (Figure 4):

1. Initialize  $p = 0$  where  $p$  is a counter that represents, at any given iteration, the number of materials (polygons) that have already been reconstructed in cell  $\Omega_{i,j}$ . The uncaptured space in this cell is initialized as

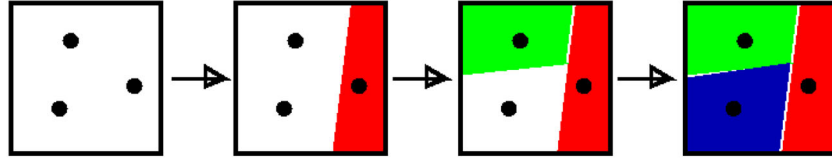


Figure 4. Illustration of volume-preserving and volume-tessellating MOF reconstruction with three materials; in order to conserve volume, the MOF reconstruction must tessellate a cell when it is used for advection (Section 3.2.3). The uncaptured region is initialized as the whole cell,  $\Omega_u^0 = \Omega_{i,j}$ , and then progressively reduced as each new material  $m$  fills the cell:  $\Omega_u^{p+1} = \Omega_u^p \cap \Omega_{m_p}^{Complement}$ . The solid circles are the reference first-order moments for each material.

$$\Omega_u^p = \Omega_{i,j} \quad (17)$$

where  $\Omega_{i,j}$  represents cell  $(i, j)$ . The centroid of  $\Omega_u^p$  is denoted as  $\mathbf{x}_u^p$ . Tag all materials as ‘not defined’.

2. In the cell, identify the material whose centroid ( $\mathbf{x}_{i,j}^m$ ) is furthest to the uncaptured centroid  $\mathbf{x}_u^p$  among all ‘not defined’ materials, that is,

$$m^p = \operatorname{argmax}_{m, F_{i,j}^m > 0, m \text{ not defined}} |\mathbf{x}_{i,j}^m - \mathbf{x}_u^p| \quad (18)$$

3. Calculate the slope  $\hat{\mathbf{n}}$  and intercept  $b$  that minimize the centroid error with the constraint that  $|F_{act}^{m^p}(\hat{\mathbf{n}}, b) - F_{ref}^{m^p}| = 0$  and construct the MOF interface.  $\Omega_{m^p}$  is defined as

$$\Omega_{m^p} = \Omega_u^p \cap \{x | \hat{\mathbf{n}} \cdot (x - \mathbf{x}_{i,j}) + b \geq 0\} \quad (19)$$

The Gauss–Newton method as written for the two-material scenario is used to solve the optimization problem. Tag material  $m$  as ‘defined’.

4. Update  $\Omega_u^{p+1}$

$$\Omega_u^{p+1} = \Omega_u^p \cap \Omega_{m^p}^{Complement} \quad (20)$$

5. Let  $p = p + 1$  and go back to step 2.

As a remark on determining volumes and moments of polygonal regions, in contrast to earlier implementations of the MOF interface reconstruction method that used a Gauss–Green discretization to compute volumes and moments of polygonal regions [31], our implementation makes use of triangulation (tetrahedralization in 3D) to compute reference volumes and reference centroids. Rectangular cells are subdivided into triangles. The intersection of two triangular (tetrahedral) regions is expressed as the union of multiple triangular (tetrahedral) regions. A lookup table is utilized to efficiently cut a triangle (tetrahedron) with a linear (planar) interface and triangulate (tetrahedralize) the cut region. Volume of the cut region is then computed as the sum of the volumes of the constituent triangles (tetrahedra). Because all polygonal (polyhedral) regions are decomposed into triangles (tetrahedra), it is easy to compute moments. For a given triangle (tetrahedra)  $T$ , the centroid  $\mathbf{x}_T$  is the average of its vertices  $\mathbf{x}_j$  shown as follows:

$$\mathbf{x}_T = \frac{\int_T \mathbf{x} \cdot d\mathbf{x}}{\int_T d\mathbf{x}} = \frac{1}{3} \sum_{j=1}^3 \mathbf{x}_j \quad (21)$$

Any polygonal region  $P$  that we consider can be written as the union of  $N$  triangles  $T_i$ ,

$$P = \bigcup_{i=1}^N T_i \quad (22)$$

If each triangle has volume  $V_i$  and centroid  $\mathbf{x}_{T_i}$ , then the volume  $V_P$  of the region  $P$  is equal to the sum of the volumes of  $T_i$ , and the centroid  $\mathbf{x}_P$  of  $P$  is the volume-weighted sum of the centroids:

$$V_P = \sum_{i=1}^N V_i \quad (23)$$

$$\mathbf{x}_P = \frac{\int_P \mathbf{x} \cdot d\mathbf{x}}{\int_P d\mathbf{x}} = \frac{\sum_{i=1}^N V_i \mathbf{x}_{T_i}}{V_P} \quad (24)$$

**3.2.2. MINMOD piecewise linear reconstruction of the momentum for each material.** Without loss of generality, we describe the piecewise linear, MINMOD slope-limited, momentum reconstruction procedure for directionally split CISL advection in the  $x$  direction in cell  $\Omega_{i,j}$ :

1. Initialize momentum for material  $m$  from density and velocity:

$$\mathbf{U}_{m,i',j}^n \equiv \rho_m \mathbf{u}_{i',j}^n \quad i' = i-1, i, i+1$$

2. Initialize the slope for the linear reconstruction:

$$\begin{aligned} \mathbf{U}'_{i,j} &= \begin{cases} 0 & (D_+ \mathbf{U}_{i,j})(D_- \mathbf{U}_{i,j}) \leq 0 \\ \text{SGN} \cdot \min \left( \left| \frac{D_+ \mathbf{U}_{i,j}}{\Delta x} \right|, \left| \frac{D_- \mathbf{U}_{i,j}}{\Delta x} \right| \right) & \text{otherwise} \end{cases} \\ D_+ \mathbf{U}_{i,j} &\equiv \mathbf{U}_{i+1,j} - \mathbf{U}_{i,j} \quad D_- \mathbf{U}_{i,j} \equiv \mathbf{U}_{i,j} - \mathbf{U}_{i-1,j} \quad \text{SGN} \equiv \frac{D_+ \mathbf{U}_{i,j}}{|D_+ \mathbf{U}_{i,j}|} \end{aligned}$$

3. The slope-limited reconstruction of the momentum for material  $m$  is now

$$\mathcal{U}_{m,i,j}^n(x) = (\mathbf{U}')_{m,i,j}^n (x - x_{m,i,j}^n) + \mathbf{U}_{m,i,j}^n \quad (25)$$

**3.2.3. Directionally split mapping of reconstructed solution into a target cell  $\Omega_{i,j}$ .** We have implemented two different directional splitting advection algorithms. The first directionally split algorithm that we implemented is based on the alternating Eulerian implicit (EI)-Lagrangian explicit (LE) algorithm described in [20] and [43]. In 2D, we advect in the  $X$  direction first using EI time discretization (backwards tracing), and then we advect in the  $Y$  direction using the LE (forwards tracing) time discretization. In 3D, the advection ordering is  $X$  (EI),  $Y$  (LE), and  $Z$  (EI). The ordering is reversed every time step so that in 2D, for this example, the next time step would involve (EI) advection in the  $Y$  direction, followed by (LE) advection in the  $X$  direction. The alternating approach exactly conserves volume for each material in 2D, but not in 3D and not using an axisymmetric  $R$ - $Z$  coordinate system.

The second directionally split algorithm that we implemented follows the algorithm described in [22]. The approach advects in the  $X$  and  $Y$  ( $X$ - $Y$ - $Z$  in 3D) directions using the EI (backwards tracing) scheme and then reverses the direction ordering at the next time step. In a given cell  $\Omega_{i,j}$ , the Weymouth and Yue algorithm for advection in 2D solves the following equations in which the initial condition at time  $t = t^n$ ,  $F^n$ , is given:

$$\begin{aligned} F_\tau + (uF)_x &= 0 \quad 0 \leq \tau \leq \Delta t \\ F_\tau + (vF)_y &= 0 \quad \Delta t \leq \tau \leq 2\Delta t \quad \text{if } F_{i,j}^n < 1/2 \\ F_\tau + (uF)_x &= u_x \quad 0 \leq \tau \leq \Delta t \\ F_\tau + (vF)_y &= v_y \quad \Delta t \leq \tau \leq 2\Delta t \quad \text{if } F_{i,j}^n \geq 1/2 \end{aligned}$$

Remarks:

- If the face velocity is discretely divergence free, then the EI-LE method is free stream preserving and conserves volume exactly in 2D.
- If the face velocity is discretely divergence free, then the Weymouth and Yue algorithm preserves volume exactly in 2D, 3D axisymmetric, and 3D coordinate systems, albeit the Weymouth and Yue algorithm has a more stringent time step constraint in 3D,

$$|U|\Delta t < \frac{\Delta x}{6}$$

than for the EI–LE approach,

$$|U|\Delta t < \frac{\Delta x}{2}$$

Here we illustrate the details for the backwards projection and forwards projection, but only in the  $x$  direction. The CISL algorithm in the  $y$  and  $z$  directions is carried out analogously.

For backwards tracing of characteristics, the CISL mapping function is

$$T_{i,j}^{CISL}(x, y) = (\alpha x + \beta, y)$$

in which  $\alpha$  and  $\beta$  are chosen so that

$$T_{i,j}^{CISL} : \Omega_{i,j}^{depart} \rightarrow \Omega_{i,j}^{target}$$

where

$$\begin{aligned} x_{Left} &= x_{i-1/2} - \Delta t u_{i-1/2} \\ x_{Right} &= x_{i+1/2} - \Delta t u_{i+1/2} \\ \Omega_{i,j}^{depart} &= \{(x, y) | x_{Left} < x < x_{Right}, y_{j-1/2} < y < y_{j+1/2}\} \\ \Omega_{i,j}^{target} &= \{(x, y) | x_{i-1/2} < x < x_{i+1/2}, y_{j-1/2} < y < y_{j+1/2}\} \\ \alpha &= \frac{\Delta x}{x_{Right} - x_{Left}} \\ \beta &= x_{i-1/2} - \alpha x_{Left}. \end{aligned}$$

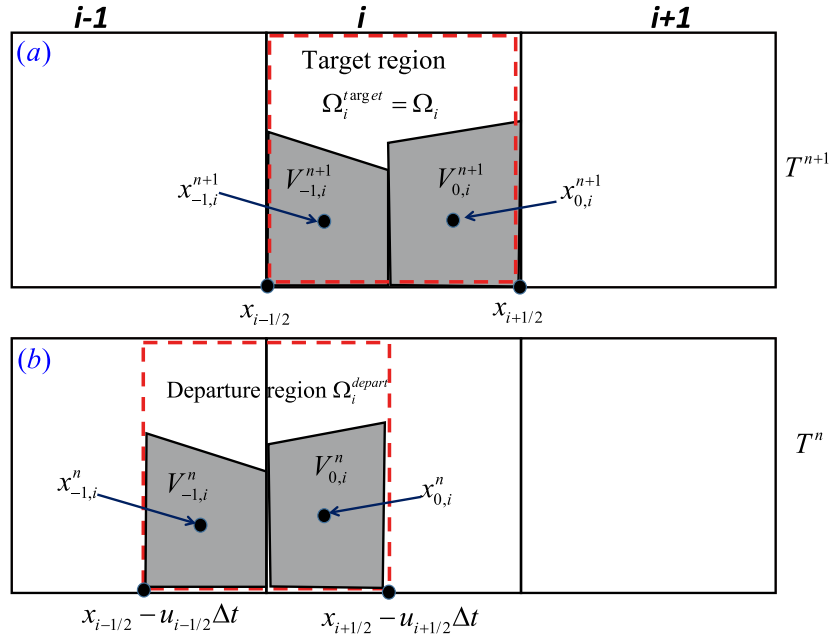


Figure 5. Backward projection for the directionally split method. The dashed rectangle in (b) represents the departure region ( $\Omega_i^{depart}$ ). We denote the departure region of material  $m$  as  $\Omega_{m,i}^{depart} = V_{-1,i}^n \cup V_{0,i}^n$ , which is shaded in (b).  $V_{-1,i}^n$  and  $V_{0,i}^n$  are the intersection of the departure region with material  $m$  in cells  $i-1$  and  $i$ , respectively, that is,  $V_{-1,i}^n \equiv \Omega_{m,i-1}^n \cap \Omega_i^{depart}$  and  $V_{0,i}^n \equiv \Omega_{m,i}^n \cap \Omega_i^{depart}$ .  $x_{-1,i}^n$  and  $x_{0,i}^n$  are the centroid of regions  $V_{-1,i}^n$  and  $V_{0,i}^n$ , respectively. The target region of material  $m$  is denoted as  $\Omega_{m,i}^{target} = V_{-1,i}^{n+1} \cup V_{0,i}^{n+1}$ , which is shaded in (a). The overall target region in (a) is cell  $i$ , and we denote this as  $\Omega_i^{target}$ .

For forwards tracing of characteristics, the mapping function is a piecewise linear function broken up into three parts,  $i' = -1, 0, 1$ :

$$T_{i,j}^{CISL}(x, y) = \begin{cases} \tilde{T}_{i-1,j}^{CISL}(x, y) & \text{if } \tilde{T}_{i-1,j}^{CISL}(x, y) \in \Omega_{i,j} \\ \tilde{T}_i^{CISL}(x, y) & \text{if } \tilde{T}_i^{CISL}(x, y) \in \Omega_{i,j} \\ \tilde{T}_{i+1,j}^{CISL}(x, y) & \text{if } \tilde{T}_{i+1,j}^{CISL}(x, y) \in \Omega_{i,j} \end{cases}$$

$$\tilde{T}_{i+i',j}^{CISL}(x, y) = (\alpha x + \beta, y)$$

$$x_{Left} = x_{i+i'-1/2} + \Delta t u_{i+i'-1/2}$$

$$x_{Right} = x_{i+i'+1/2} + \Delta t u_{i+i'+1/2}$$

$$\alpha = \frac{x_{Right} - x_{Left}}{\Delta x}$$

$$\beta = x_{Left} - \alpha x_{i+i'-1/2}.$$

In Figures 5 and 6, we illustrate the backwards and forwards tracing of characteristics, respectively. In Figure 5, the departure region

$$\Omega_{i,j}^{depart} \equiv (T_{i,j}^{CISL})^{-1}(\Omega_{i,j})$$

is intersected with each reconstructed (polygonal) material region in neighboring cells; this is denoted by  $V_{-1,i}^n$  and  $V_{0,i}^n$  in Figure 5. Then these material regions, and the momentum within these regions, are mapped forward under the action of  $T_{i,j}^{CISL}$  in order to form the material regions at the new time:

$$V_{-1,i}^{n+1} = T_{i,j}^{CISL}(V_{-1,i}^n)$$

$$V_{0,i}^{n+1} = T_{i,j}^{CISL}(V_{0,i}^n)$$

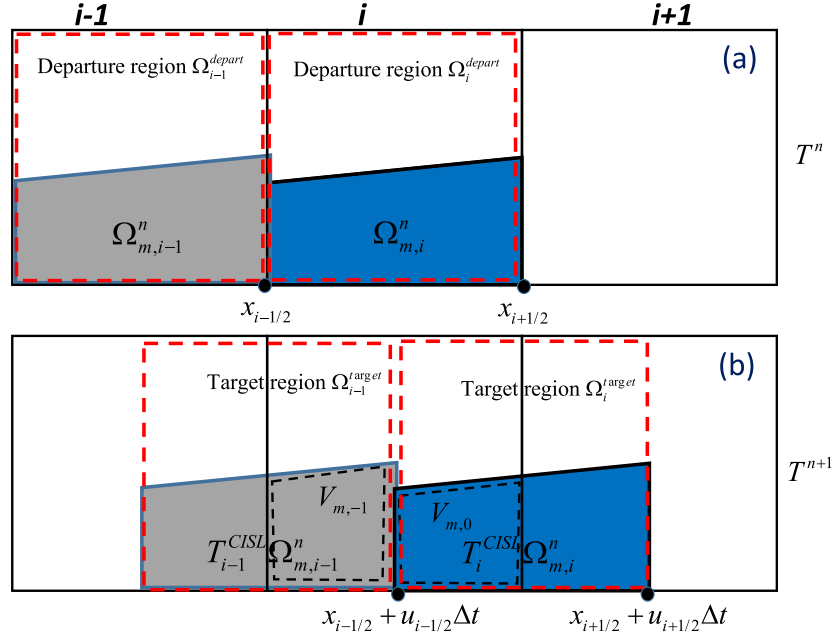


Figure 6. Forward projection for the directionally split method. The dashed rectangles in (b) represent the target regions ( $\Omega_{i-1}^{target}$  and  $\Omega_i^{target}$ ). The departure regions are cells  $i - 1$  and  $i$  in (a). The departure regions of material  $m$  in cells  $i - 1$  and  $i$  are  $\Omega_{m,i-1}^n$  and  $\Omega_{m,i}^n$ , respectively. The target regions of material  $m$  are  $\tilde{T}_{i-1}^{CISL}\Omega_{m,i-1}^n$  and  $\tilde{T}_i^{CISL}\Omega_{m,i}^n$ .  $V_{m,-1}$  and  $V_{m,0}$  are the overlapping regions of the target regions with cell  $i$ , that is,  $V_{m,-1} \equiv \tilde{T}_{i-1}^{CISL}(\Omega_{m,i-1}^n) \cap \Omega_i$  and  $V_{m,0} \equiv \tilde{T}_i^{CISL}(\Omega_{m,i}^n) \cap \Omega_i$ .

So, for either the forwards or backwards tracing algorithm, we solve the volume fraction equation (10), centroid equation, and momentum advection equation (9), as follows:

$$F_{m,i,j}^{n+1} = \frac{\sum_{i'=-1}^1 |T_{i,j}^{CISL}(\Omega_{m,i+i'}^n) \cap \Omega_{i,j}|}{|\Omega_{i,j}|} \quad (26)$$

$$\mathbf{x}_{m,i,j}^{n+1} = \frac{\sum_{i'=-1}^1 \int_{T_{i,j}^{CISL}(\Omega_{m,i+i'}^n) \cap \Omega_{i,j}} \mathbf{x} d\mathbf{x}}{F_{m,i,j}^{n+1} |\Omega_{i,j}|} \quad (27)$$

$$\mathbf{u}_{m,i,j}^{advect} = \frac{\sum_{i'=-1}^1 \int_{\Omega_{m,i+i'}^n \cap (T_{i,j}^{CISL})^{-1}(\Omega_{i,j})} \mathcal{U}_{m,i+i',j}^n(x) d\mathbf{x}}{\sum_{i'=-1}^1 \rho_m |\Omega_{m,i+i'}^n \cap (T_{i,j}^{CISL})^{-1}(\Omega_{i,j})|} \quad (28)$$

### 3.3. Distance functions

In order to approximate the curvature of interfaces (Section 3.5), signed distance functions  $\phi_{m,i,j}$  are constructed.  $\phi_{m,i,j}$  is the signed distance from the center of cell  $\Omega_{i,j}$ ,  $\mathbf{x}_{i,j}$ , to the piecewise linear (planar in 3D) ‘tessellating’ (in the vicinity of contact lines) or ‘non-tessellating’ (in the

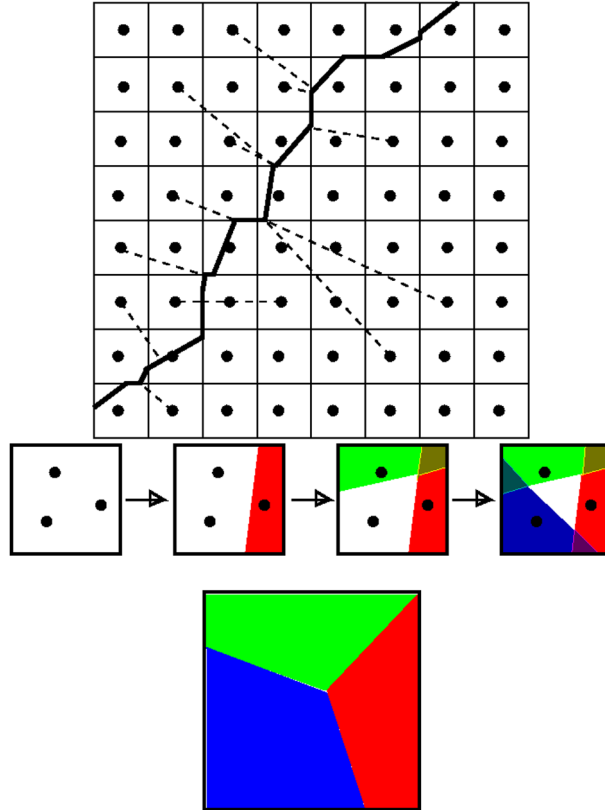


Figure 7. Top: Signed distance functions  $\phi_m$  are the exact signed distance to the piecewise linear non-tessellating moment-of-fluid (MOF) reconstructed interface.  $\phi_m$  is used to find the curvature (Section 3.5). Middle: Illustration of non-tessellating MOF reconstruction. The uncaptured region for each new material is always the whole cell:  $\Omega_u = \Omega_{i,j}$ . The solid circles are the reference centroids for each material. Bottom: The non-tessellating distance functions are projected onto tessellating distance functions in cells containing a triple junction (29).

vicinity of triple junctions) MOF reconstructed material  $m$  interface (Figure 7). The sign is positive if  $\mathbf{x}_{i,j} \in \Omega_{m,i,j}$  and negative otherwise.

At a triple point in cell  $\Omega_{i,j}$ , the ‘non-tessellating’ MOF reconstructed interface is formed as follows (Figure 7):

For each material  $m$  ( $m = 1, \dots, M$ ), if  $F_m > 0$ , then we find the slope  $\hat{\mathbf{n}}$  and intercept  $b$  that minimize the centroid error with the constraint that  $|F_{act}^m(\hat{\mathbf{n}}, b) - F_{ref}^m| = 0$ .

The Gauss–Newton method as written in Section 3.2.1 is used to solve the optimization problem. The minimization problem is carried out assuming, for each  $m = 1, \dots, M$ , that the uncaptured space  $\Omega_u$  (17) is the whole cell:  $\Omega_u = \Omega_{i,j}$ . In comparing Figure 4 with Figure 7, we illustrate the difference between the MOF reconstruction that tessellates a cell and the MOF reconstruction that is not required to tessellate a cell.

Once the piecewise linear (planar in 3D) interfaces are reconstructed, then we find the exact signed distance to these reconstructed interfaces [26].

Remarks:

- As in [44], the signed distance functions  $\phi_m$  representing fluid materials are extrapolated into rigid boundaries. When creating the signed distance to material  $m$ , where  $m$  represents a fluid, we ignore interfaces that separate  $m$  from rigid boundaries. The extrapolated value of  $\phi_{m,i,j}$ , where  $\mathbf{x}_{i,j}$  is inside a rigid-body material, is taken as the value of  $\phi_{m,i',j'}$ , where  $\mathbf{x}_{i',j'}$  is the closest cell outside the rigid body to  $\mathbf{x}_{i,j}$ . See Figure 8.
- It is possible for  $\phi_m$  to be positive for more than one value of  $m$ , and it is also possible that  $\phi_m < 0$  for all values of  $m$ , so in computational cells  $\Omega_{i,j}$  containing a triple junction, we project these distance functions to tessellating distance functions as follows:

$$\phi_m \leftarrow \begin{cases} \phi_m & \text{if } \phi_m \geq 0 \text{ and } m = \operatorname{argmax}_{m'} F_{m'} \\ \phi_m & \text{if } \phi_m < 0 \text{ and } m \neq \operatorname{argmax}_{m'} F_{m'} \\ -\epsilon \Delta x & \text{if } \phi_m \geq 0 \text{ and } m \neq \operatorname{argmax}_{m'} F_{m'} \\ \epsilon \Delta x & \text{if } \phi_m < 0 \text{ and } m = \operatorname{argmax}_{m'} F_{m'} \end{cases} \quad m = 1, \dots, M \quad (29)$$

We assign  $\epsilon = 0.01$  in all of our sample calculations.

### 3.4. Viscosity forces

The viscosity force,  $\mathbf{F}^{viscous}$ , is discretized using a sub-cycling algorithm [37]:

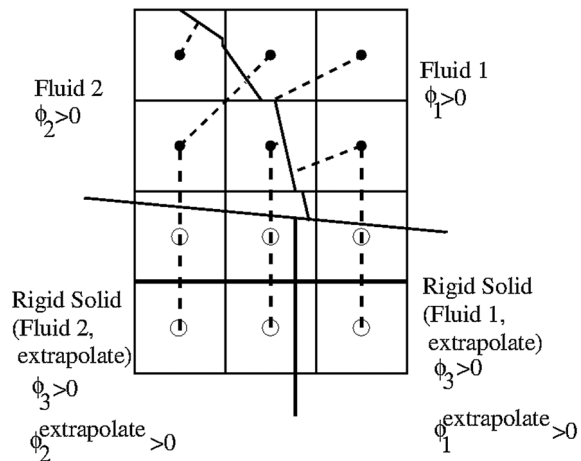


Figure 8. When constructing the distance functions  $\phi_1$  and  $\phi_2$  outside of the rigid boundary ( $\phi_3 < 0$ ), the rigid boundary interface is ignored. The thin dashed lines represent the closest distance to the interface separating materials 1 and 2. The values of  $\phi_1$  and  $\phi_2$  where  $\phi_3 \geq 0$  are extrapolated from the nearest cell in which  $\phi_3 < 0$  (thick dashed lines). The extrapolated fluid interface is the thick solid line.

1. Determine the number of sub-cycling steps,  $K$ , such that the following stability condition is satisfied:

$$\frac{\Delta t}{K} \leq \max_{m=1,\dots,M} \frac{\rho_m}{2\text{DIM}\mu_m} \Delta x^2$$

2.  $\mathbf{u}^{(0)} = \mathbf{u}^{\text{advect}}$
3. For  $k = 1, \dots, K$ ,

$$\mathbf{u}^{(k)} = \mathbf{u}^{(k-1)} + \frac{\Delta t}{K} \frac{\nabla \cdot (2\mu^{n+1} D^{(k-1)})}{\rho^{n+1}} \quad (30)$$

4.  $\mathbf{F}^{\text{viscous}} = (\mathbf{u}^{(K)} - \mathbf{u}^{\text{advect}})/\Delta t$ .

Remarks:

- $\rho^{n+1}$  (30) is written in terms of the volume fractions in multimaterial cells  $\Omega_{i,j}$ :

$$\rho_{i,j}^{n+1} = \sum_{m=1}^M \rho_m F_{m,i,j}^{n+1} \quad (31)$$

- $\mu^{n+1}$  (30) is written in terms of the half-volume fractions at multimaterial faces  $\Omega_{i+1/2,j}$ :

$$\mu_{i+1/2} = \frac{\Omega_{i+1/2,j}}{\sum_{m=1}^M \frac{1}{\mu_m} (|\Omega_{i,j}^m \cap \Omega_{i,R}| + |\Omega_{i+1,j}^m \cap \Omega_{i+1,L}|)}$$

The regions  $\Omega_{i+1/2,j}$ ,  $\Omega_{i,R}$ , and  $\Omega_{i+1,L}$  are illustrated in Figure 9.

- The spatial discretization of  $D^{(k-1)} = (\nabla \mathbf{u}^{(k-1)} + (\nabla \mathbf{u}^{(k-1)})^T)/2$  is the same as that described in section 3 of [45] in which all terms are discretized using second-order central differencing except for the coupling terms in the vicinity of interface(s) separating multiple materials.

### 3.5. Surface tension

The spatial discretization of the surface tension force corresponds to the ghost fluid method [46] when two materials are present. The surface tension force

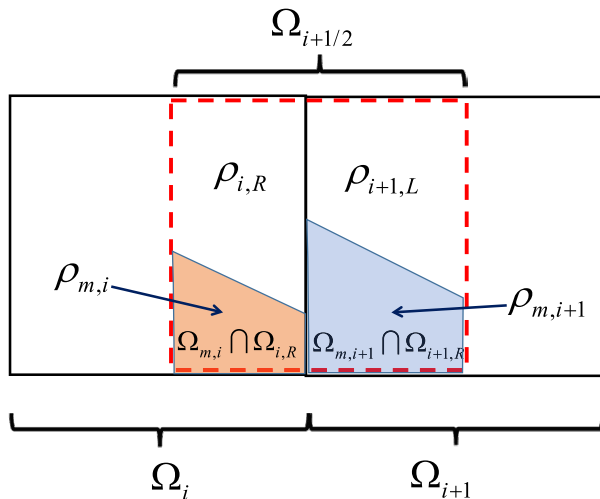


Figure 9. To compute the half-cell densities  $\rho_{i,R}$  and  $\rho_{i+1,L}$  in cut cells, the moment-of-fluid reconstructed interface is used to determine the half-cell volume fractions  $F_{m,i,R}$  and  $F_{m,i+1,L}$ , so that one can derive  $\rho_{i,R} = \sum_m F_{m,i,R} \rho_{m,i}$  and  $\rho_{i+1,L} = \sum_m F_{m,i+1,L} \rho_{m,i+1}$ .

$$-\Delta t \frac{\sigma \kappa \nabla H}{\rho}$$

is discretized at cell faces as

$$\mathbf{F}_{i+1/2,j}^{MAC,tension} \equiv -\Delta t \frac{\sigma \kappa_{i+1/2,j} (H(\phi_{i+1,j}) - H(\phi_{i,j}))}{\rho_{i+1/2,j}^{n+1} \Delta x} \quad (32)$$

where  $H(\phi)$  is the Heaviside function (5),  $\phi$  is a signed distance function, and  $\kappa_{i+1/2,j}$  is the curvature at the point on the interface that crosses in between cells  $\Omega_{i+1,j}$  and  $\Omega_{i,j}$ .  $\rho_{i+1/2,j}^{n+1} \equiv (\rho_{i,R} + \rho_{i+1,L})/2$  is the density for the face control volume  $\Omega_{i+1/2,j}$ .  $\rho_{i,R}$  and  $\rho_{i+1,L}$  are half-cell densities (Equations (46) and (47)).

The surface tension force is discretized at cell centers as

$$\mathbf{F}_{i,j}^{tension} \equiv \frac{\rho_{i,R} \mathbf{F}_{i+1/2,j}^{MAC,tension} + \rho_{i,L} \mathbf{F}_{i-1/2,j}^{MAC,tension}}{2\rho_{i,j}^{n+1}} \quad (33)$$

The level set height function method [44, 47] is used to approximate the curvature,  $\kappa_{i+1/2,j}$ , away from triple points and contact lines. Referring to Figure 10,  $\kappa_{i+1/2,j}$  in (32) is approximated as follows:

$$\kappa_{i\pm 1/2,j} = \begin{cases} \kappa_{i,j} & |\phi_{i,j}| < |\phi_{i\pm 1,j}| \\ \kappa_{i\pm 1,j} & \text{otherwise} \end{cases} \quad (34)$$

$$h'' \approx \frac{h_{i+1} - 2h_i + h_{i-1}}{\Delta x^2} \quad h' \approx \frac{h_{i+1} - h_{i-1}}{2\Delta x} \quad (35)$$

$$\kappa_{i,j} = \frac{-h''}{(1 + (h')^2)^{3/2}} \quad (36)$$

If the  $3 \times 3$  stencil about cell  $(i, j)$  in (34) contains a third material, then  $\kappa_{i+1/2,j}$  is approximated using central difference techniques:

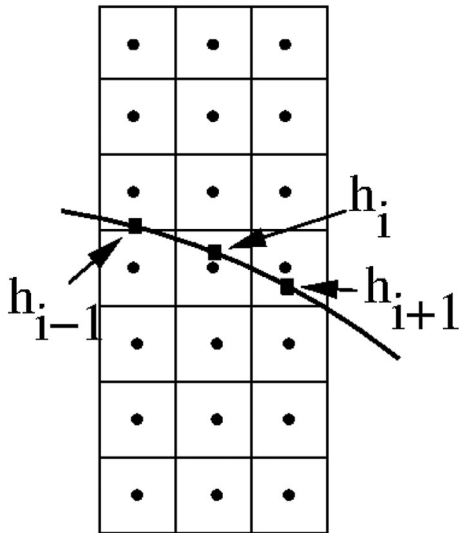


Figure 10. The level set height function method is used to approximate the curvature of the interface. The square symbols are located at the zero crossings of  $\phi$ ; for example,  $h_i = (1 - \theta_{i,j+1/2})y_j + \theta_{i,j+1/2}y_{j+1}$  where  $\theta_{i,j+1/2} \equiv \frac{|\phi_{i,j}|}{|\phi_{i,j}| + |\phi_{i,j+1}|}$ .

**Stencil contains rigid boundary.** Referring to Figure 11, if the  $3 \times 3$  stencil contains a third rigid material,  $m = 3$ , then we approximate the curvature  $\kappa_{i,j}$  in (34) as follows:

$$\kappa_{i,j} = \nabla \cdot (H(\phi_3)\mathbf{n}_{ghost} + (1 - H(\phi_3))\mathbf{n}) \quad (37)$$

$$H(\phi_3)_{i+1/2,j+1/2} = \begin{cases} 0 & \phi_{3,i+i',j+j'} \leq 0, \text{ all } i', j' = 0, 1 \\ 1 & \text{otherwise} \end{cases} \quad (38)$$

$\mathbf{n}_{ghost}$  is defined as follows (Equations [44]):

$$\begin{aligned} \tilde{\phi} &\equiv \frac{\phi_1 - \phi_2}{2} \\ \mathbf{n}_3 &= -\frac{\nabla \phi_3}{|\nabla \phi_3|} \quad \mathbf{n} = \frac{\nabla \tilde{\phi}}{|\nabla \tilde{\phi}|} \\ \mathbf{t}_1 &= \mathbf{n}_3 \times \mathbf{n} \quad \mathbf{t}_2 = \mathbf{n}_3 \times \mathbf{t}_1 \\ \bar{\mathbf{n}}_{ghost} &= \text{sign}(\mathbf{n}_3 \cdot \mathbf{t}_2) \sin(\theta) \frac{\mathbf{t}_2}{|\mathbf{t}_2|} - \cos(\theta) \mathbf{n} \quad \mathbf{n}_{ghost} = \frac{\bar{\mathbf{n}}_{ghost}}{|\bar{\mathbf{n}}_{ghost}|} \end{aligned}$$

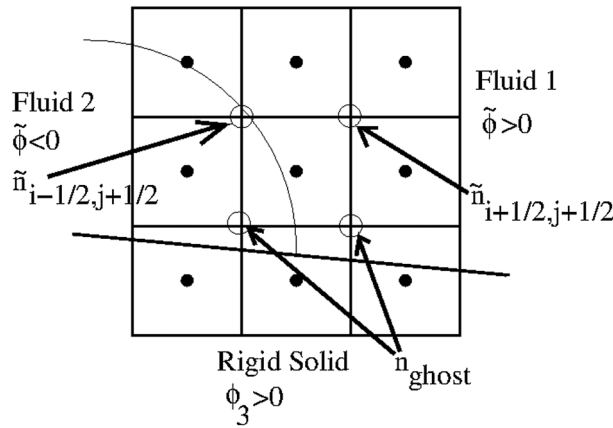


Figure 11. Illustration of the  $3 \times 3$  stencil used to calculate the curvature  $\kappa_i$  when the stencil contains a rigid material (material 3). Given the  $3 \times 3$  stencil of values for the distance function  $\tilde{\phi}_{i+i',j+j'}, i' = -1, 0, 1, j' = -1, 0, 1$  ( $\tilde{\phi} \equiv (1/2)(\phi_1 - \phi_2)$ ), the central difference curvature discretization technique is used (Equation (37)).  $\phi_3$  and  $\phi$  are defined at the closed circles, and the normals  $\mathbf{n}_{ghost}$  and  $\tilde{\mathbf{n}}$  are defined at the open circles.

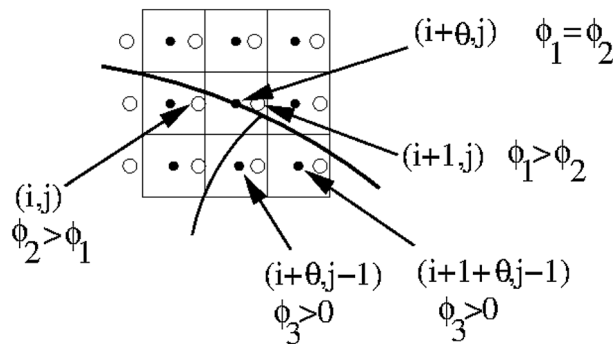


Figure 12. Illustration of the  $3 \times 3$  stencil used to calculate the curvature  $\kappa_{i+1/2,j}$  when the stencil contains a third fluid material (material 3 in this diagram).  $(i + \theta, j)$  is the  $\Gamma_{1,2}$  interface crossing between cells  $(i, j)$  and  $(i + 1, j)$  ( $\theta = |\tilde{\phi}_i|/(|\tilde{\phi}_i| + |\tilde{\phi}_{i+1}|)$ ,  $\tilde{\phi} = (1/2)(\phi_1 - \phi_2)$ ). Given a  $4 \times 3$  stencil of distance function values,  $\phi_{i+i',j+j'}, i' = -1, \dots, 2, j' = -1, 0, 1$  (open circles), the distance functions are first interpolated to a  $3 \times 3$  stencil (filled circles) centered at  $(i + \theta, j)$ . Then given the  $3 \times 3$  stencil of values for the distance functions  $\phi_{i+\theta+i',j+j'}, i' = -1, 0, 1, j' = -1, 0, 1$ , the central difference curvature discretization technique is used (Equation (40)).

**Stencil contains third fluid** Referring to Figure 12, if the  $3 \times 3$  stencil contains a third fluid,  $m = 3$ , the distance functions  $\phi_1$  and  $\phi_2$  are linearly interpolated to the  $3 \times 3$  stencil centered at the point  $(i + \theta, j)$  where

$$\theta = \frac{|\tilde{\phi}_{i,j}|}{|\tilde{\phi}_{i,j}| + |\tilde{\phi}_{i+1,j}|} \quad \tilde{\phi} \equiv \frac{\phi_1 - \phi_2}{2} \quad (39)$$

Then we discretize the curvature using central differences

$$\kappa_{i+1/2,j} = \frac{\gamma_1 \nabla \cdot \frac{\nabla \phi_1}{|\nabla \phi_1|} - \gamma_2 \nabla \cdot \frac{\nabla \phi_2}{|\nabla \phi_2|}}{\sigma_{12}}$$

where  $\gamma$  is defined in (6) and (7).  $\nabla \phi$  is discretized at the nodes surrounding cell  $(i + \theta, j)$ ; for example,

$$(\phi_x)_{i+\theta+1/2,j+1/2} \approx \frac{\phi_{i+\theta+1,j} + \phi_{i+\theta+1,j+1} - \phi_{i+\theta,j} - \phi_{i+\theta,j+1}}{2\Delta x} \quad (40)$$

### 3.6. Approximate projection method

Given the cell-centered velocity field  $\mathbf{V}$ ,

$$\mathbf{V} = \mathbf{u}^{\text{advec}} + \Delta t (\mathbf{F}^{\text{viscous}} + \mathbf{F}^{\text{tension}} + \mathbf{g})$$

we ‘approximately’ project this velocity field onto the space of divergence-free velocity fields.

1. Interpolate  $\mathbf{V}$  from cell centers to cell faces:

$$\mathbf{V}^{\text{MAC}} = \mathcal{I}(\mathbf{V} - \mathbf{F}^{\text{tension}}) + \mathbf{F}^{\text{MAC,tension}} \quad (41)$$

where  $\mathcal{I}$  is a momentum-preserving interpolation operator [35, 48] and the discretized surface tension forces  $\mathbf{F}^{\text{tension}}$  and  $\mathbf{F}^{\text{MAC,tension}}$  are defined by equations (32) and (33).

2. Project  $\mathbf{V}^{\text{MAC}}$  exactly onto the space of discretely divergence-free velocity fields:

$$\mathbf{u}^{\text{MAC},n+1} = \mathbf{V}^{\text{MAC}} - \Delta t \frac{\nabla p}{\rho^{n+1}} \quad (42)$$

$$\nabla \cdot \frac{\nabla p}{\rho^{n+1}} = \frac{\nabla \cdot \mathbf{V}^{\text{MAC}}}{\Delta t} \quad (43)$$

3. Interpolate the pressure  $p$  found in (43) from cell centers to face centers using the condition of constant contact [35, 48] and then update the new cell-centered velocity:

$$\mathbf{u} = \mathbf{V} - \Delta t \frac{\nabla p^{\text{MAC}}}{\rho^{n+1}} \quad (44)$$

Remarks:

- We call our method an ‘approximate projection method’ [21, 49] because, although the process of deriving  $\mathbf{u}^{\text{MAC},n+1}$  from  $\mathbf{V}^{\text{MAC}}$  is an exact projection [50, 51], that is,

$$\mathbf{u}^{\text{MAC},n+1} \equiv \mathcal{P}^{\text{MAC}} \mathbf{V}^{\text{MAC}} \quad \mathcal{P}^{\text{MAC}} = (\mathcal{P}^{\text{MAC}})^2 \quad \mathcal{P}^{\text{MAC}} \perp \mathcal{I} - \mathcal{P}^{\text{MAC}}$$

the process of deriving  $\mathbf{u}^{n+1}$  from  $\mathbf{V}$  is not an exact projection. In other words, if we implicitly define  $\mathcal{P}$  as

$$\mathbf{u}^{n+1} \equiv \mathcal{P} \mathbf{V}$$

it is not necessarily true that  $\mathcal{P} = (\mathcal{P})^2$  or that  $\mathcal{P} \perp \mathcal{I} - \mathcal{P}$ .

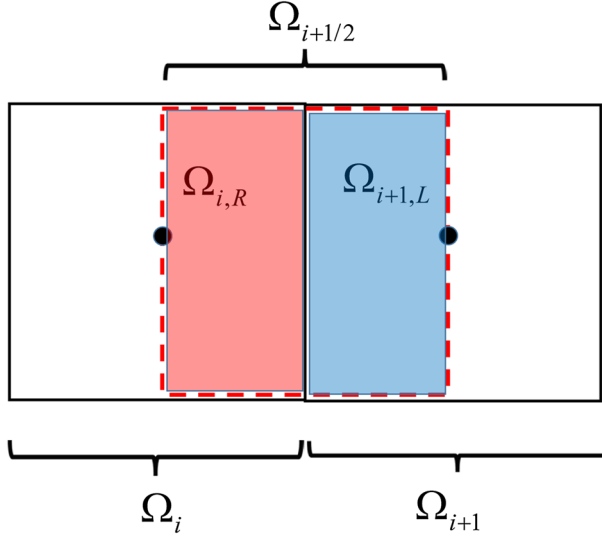


Figure 13. Left and right control volumes  $\Omega_{i,R}$  and  $\Omega_{i+1,L}$ , with face-centered control volume  $\Omega_{i+1/2}$ . Cell centers are shown as dots, and the boundary of the face-centered control volume is shown as dashes.

- The interpolation operator  $\mathcal{I}$  (41) is a mass-weighted interpolation from cell control volumes to face control volumes. The cell  $\Omega_{i,j}$  is separated into left and right control volumes, for example,  $\Omega_{i,L}$  and  $\Omega_{i,R}$  for interpolating the horizontal velocity. The interpolation of cell-centered velocity to cell faces should respect conservation of momentum, so it is required that the integral over all face-centered control volumes (45) be equal to the integral over all cells. We define the face control volume  $\Omega_{i+1/2}$  as

$$\Omega_{i+1/2} = \Omega_{i,R} \cup \Omega_{i+1,L} \quad (45)$$

where  $\Omega_{i,R}$  is the right half control volume of cell  $i$  and  $\Omega_{i+1,L}$  is the left half control volume of cell  $i + 1$  as illustrated in Figure 13. The density over each half control volume is derived from the MOF linearly reconstructed interface:

$$\rho_{i,R} = \frac{1}{|\Omega_{i,R}|} \sum_{m=1}^M |\Omega_{m,i} \cap \Omega_{i,R}| \rho_m \quad (46)$$

$$\rho_{i+1,L} = \frac{1}{|\Omega_{i+1,L}|} \sum_{m=1}^M |\Omega_{m,i+1} \cap \Omega_{i+1,L}| \rho_m \quad (47)$$

The face-centered density  $\rho_{i+1/2}$  is defined as the mass in the half-cell regions  $\Omega_{i,R}$  and  $\Omega_{i+1,L}$  divided by the volume of the face-centered control volume  $\Omega_{i+1/2}$  (48),

$$\rho_{i+1/2} = \frac{\rho_{i,R} |\Omega_{i,R}| + \rho_{i+1,L} |\Omega_{i+1,L}|}{|\Omega_{i+1/2}|} \quad (48)$$

The face-centered velocity that is to be projected (41) is now defined as a mass-weighted interpolation of the cell-centered velocity that is to be projected, for example,

$$u_{i+1/2} = \frac{u_i \rho_{i,R} |\Omega_{i,R}| + u_{i+1} \rho_{i+1,L} |\Omega_{i+1,L}|}{\rho_{i+1/2} |\Omega_{i+1/2}|} \quad (49)$$

- The finite-volume method is used to discretize (43). For example,

$$\begin{aligned}(\nabla \cdot V^{MAC})_{i,j} &\approx \frac{u_{i+1/2,j} - u_{i-1/2,j}}{\Delta x} + \frac{v_{i,j+1/2} - v_{i,j-1/2}}{\Delta y} \\(p_x/\rho)_{i+1/2,j} &\approx \frac{p_{i+1,j} - p_{i,j}}{\rho_{i+1/2,j} \Delta x}\end{aligned}$$

- The cell-averaged momentum is updated in a conservative fashion (44). It is required to interpolate the cell-centered pressure to the cell faces. As in [35, 48], we define the momentum equation in each half-cell region,  $\Omega_{i,R}$  and  $\Omega_{i+1,L}$ :

$$\frac{Du_{i,R}}{Dt} = \frac{u_{i,R}^{n+1} - u_{i,R}^*}{\Delta t} = -\frac{p_{i+1/2} - p_i}{\rho_{i,R} \Delta x / 2} \quad (50)$$

and

$$\frac{Du_{i+1,L}}{Dt} = \frac{u_{i+1,L}^{n+1} - u_{i+1,L}^*}{\Delta t} = -\frac{p_{i+1}^{n+1} - p_{i+1/2}^{n+1}}{\rho_{i+1,L} \Delta x / 2} \quad (51)$$

We apply the constraint that the interface between cells must remain in contact [48]; that is,  $\frac{Du_{i,R}}{Dt} = \frac{Du_{i+1,L}}{Dt}$ . Using this constraint and equations (50) and (51), the pressure at the cell face  $p_{i+1/2}$  (52) is found:

$$p_{i+1/2} = \frac{\rho_{i,R} p_{i+1} + \rho_{i+1,L} p_i}{\rho_{i,R} + \rho_{i+1,L}} \quad (52)$$

The derivations of the half-cell densities  $\rho_{i,R}$  and  $\rho_{i+1,L}$  are given by (46) and (47). With pressure defined at cell faces, we can conservatively update the cell-averaged momentum, for example, for the horizontal velocity (53):

$$u_i^{n+1} = u_i^* - \Delta t \frac{p_{i+1/2}^{n+1} - p_{i-1/2}^{n+1}}{\rho_i \Delta x} \quad (53)$$

#### 4. RESULTS AND DISCUSSION

The time step,  $\Delta t$ , is chosen according to the following scheme:

$$\Delta t = \min(\Delta t^{advect}, \Delta t^{tension}) \quad (54)$$

$$\Delta t^{advect} = CFL \frac{\Delta x}{\max_{i,j} |u_{i,j}|} \quad (55)$$

$$\Delta t^{tension} = \min_{m,n} \frac{\Delta x^{3/2}}{\sqrt{\frac{2\pi\sigma_{m,n}}{\rho_m + \rho_n}}} \quad (56)$$

If the Weymouth and Yue [22] directionally split algorithm is used, then,

$$CFL = \frac{1}{2\text{DIM}} \quad (57)$$

where ‘DIM’ is 2 or 3. If the EI-LE [20, 43] directionally split algorithm is used, then  $CFL = 1/2$ .

We use dynamic block-structured AMR in order to define the computational grid [17, 52]. A computational domain that is organized using AMR is made up of a hierarchy of adaptive levels  $\ell = 0, \dots, \ell^{\max}$  with each level being the union of disjoint rectangular grids. Level  $\ell = 0$  is the coarsest level, and the mesh size on each finer level is half the mesh size of the preceding level,  $\Delta x^{\ell+1} = \Delta x^\ell / 2$ .

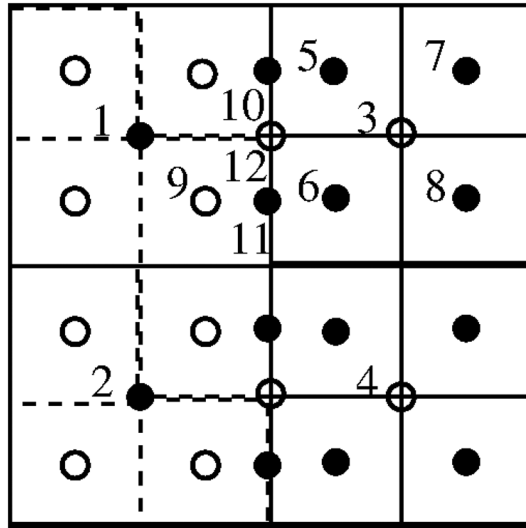


Figure 14. Illustration of a coarse/fine interface on an adaptive mesh refinement grid. Filled circles represent cells or faces not hidden by a finer mesh. Open circles are either hidden coarse-level cells or faces or fictitious fine-grid cells.

Referring to Figure 14, filled circles represent cells or faces not hidden by a finer mesh. Open circles are either hidden coarse-level cells or faces or fictitious fine-grid cells. The solution at cells or faces corresponding to open circles are interpolated from the solution at cells or faces corresponding to filled circles. Coarse and fine levels are synchronized by ‘averaging down’ the fine-level solution onto the coarser level. For example, the hidden coarse-grid cell value at cell ‘3’ is the volume-weighted average of the finer-level cells ‘5’, ‘6’, ‘7’, and ‘8’. It could be that the stencil for the fine-level cell 6 includes the fictitious fine-level cell ‘9’. In this case, the fictitious cell 9 value is interpolated from the coarse-level values at cells ‘1’, ‘2’, ‘3’, and ‘4’. The algorithm used for interpolating volume fraction and moment data from coarse levels to fine levels and the algorithm used for averaging down volume fraction and moment data from fine-level cells to hidden coarse-level cells are identical to that reported in [21].

Momentum and pressure are interpolated from coarse to fine levels using piecewise constant interpolation. This is in contrast to our recent work in [35], in which conservative MINMOD-limited second-order interpolation was used for momentum, and bilinear interpolation was used for interpolating pressure from the coarse-grid to fine-grid ghost cells. The reason we choose piecewise constant interpolation is because we find little difference in accuracy when computing the example calculations in this paper, and the piecewise constant interpolation for pressure leads to a symmetric matrix system for discretizing (43), which can be inverted quickly [53]. When piecewise constant interpolation is used for pressure, it is important that the gravitational force is expressed as

$$\mathbf{F}^{\text{gravity}} = \nabla p_{\text{hydro}}(z), \quad p_{\text{hydro}}(z) = gz \quad (58)$$

and then the gradient operator in (58) is discretized the same as that in (42) and (44).

We simulate the following cases using the proposed method to illustrate its robustness and accuracy. These test problems are as follows: (i) severe 2D and 3D deformation of three materials in a prescribed deformational flow field; (ii) relaxation to static shape for a 2D droplet on a slope; (iii) the liquid lens triple-point problem; (iv) downward liquid jets; (v) upward liquid jets; (vi) binary collision of two water drops; (vii) binary collisions of a water drop and a diesel drop; (viii) droplet impingement onto a thin liquid film; and (ix) droplet impingement onto a smooth solid wall.

#### 4.1. Severe two-dimensional and three-dimensional multimaterial deformation in a prescribed deformational flow field

We first test our multimaterial reconstruction and advection algorithms for interface deformation in a prescribed flow field. In the results that follow, we compare the computed solution with the exact solution using the symmetric difference error. We define  $\Omega_C$  and  $\Omega_E$  to be the computed and exact regions, respectively, of a deforming material in the domain. The symmetric difference error is then

$$E_{sym} = |\Omega_C \cup \Omega_E - \Omega_C \cap \Omega_E| \quad (59)$$

Equation (59) can also be defined as

$$E_{sym} = \sum_{i,j} \int_{\Omega_{i,j}} |H(\mathbf{n} \cdot (\mathbf{x} - \mathbf{x}_{i,j}) + b) - H(\phi_E(\mathbf{x}))| d\mathbf{x} \quad (60)$$

$H$  is the Heaviside function (5),  $\mathbf{n}$  and  $b$  are derived from the interface reconstruction (12),  $\mathbf{x}_{i,j}$  is the center of the cell  $\Omega_{i,j}$ , and the zero level set of  $\phi_E(\mathbf{x})$  is the exact interface location.

We compute the symmetric difference error by approximating the integral in (60) using adaptive quadrature.

**4.1.1. Two-dimensional single vortex.** In this test, a circle of radius  $R_0 = 0.15$  and center  $(0.5, 0.75)$  is placed inside a unit-sized box. The velocity field is given by the stream function [51]

$$\Psi(x, y, t) = \frac{1}{\pi} \sin^2(\pi x) \sin^2(\pi y) \cos\left(\frac{\pi t}{T}\right) \quad (61)$$

where  $T = 8$  is the period of the reversing vortical flow.

The resulting velocity field first stretches the circle into an ever thinner filament that wraps around the center of the box and then, after time  $t = T/2$ , slowly reverses and pulls the filament back into the initial circular shape at time  $t = T$ .

For this test, we prescribe the velocity at the cell faces in terms of finite differences of the exact stream function  $\Psi$  (61).

In Table I, we compare the error at  $t = T$  ( $T = 8$ ),  $E_{sym}$  (Equation (59)), for the following two cases: (i) Weymouth and Yue advection strategy [22] in which the initial circle is artificially cut in half along the vertical axis and (ii) alternating EI–LE advection strategy [20, 43] also in which the initial circle is artificially cut in half along the vertical axis.

The results using the Weymouth and Yue advection strategy on a  $512 \times 512$  grid are illustrated in Figures 15 and 16. For comparison purposes, we also show the results for the deformation of the circle in which the initial circle is not artificially cut in half. We note that both advection strategies give comparable errors on the finest mesh, but the alternating EI–LE strategy is twice as fast because the CFL condition is more lenient than that for the Weymouth and Yue advection strategy. We also note that as the grid is refined, the error for the three-material deformation problem approaches the error of the two-material case.

Table I. Symmetric difference error from Section 4.1.1, for the reversible two-dimensional vortex.

Size	Three-material Weymouth and Yue	Three-material Eulerian implicit–Lagrangian explicit	Two-material Weymouth and Yue
128	7.6E–3	2.4E–3	1.0E–3
256	1.4E–3	6.4E–4	7.1E–5
512	3.2E–5	3.2E–5	1.8E–5

Errors are taken at the end time  $t = T$ .

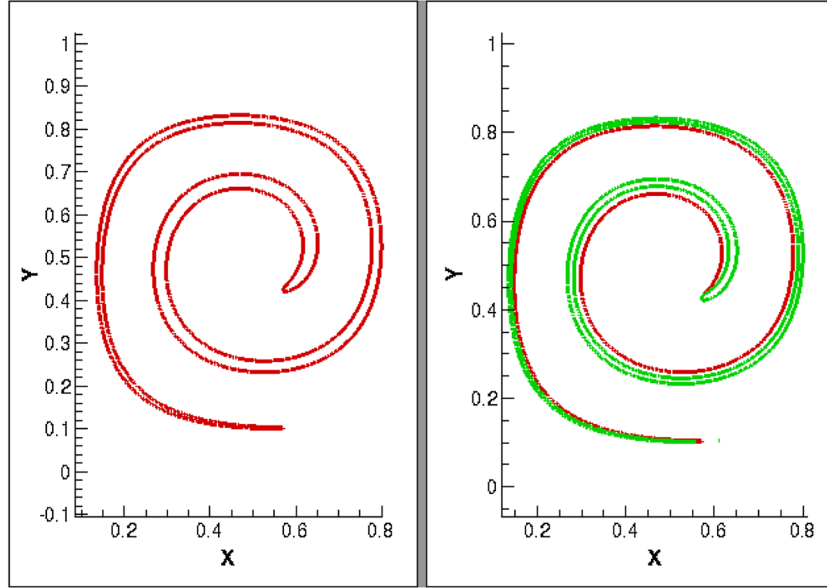


Figure 15. Deformation problem with period  $T = 8$ . Results at  $t = 4.0$ . Left: two materials. Right: three materials. The corresponding piecewise linear reconstructed interface is plotted. Base grid  $64 \times 64$ . Three levels of adaptive mesh refinement; effective fine-grid resolution  $512 \times 512$ .

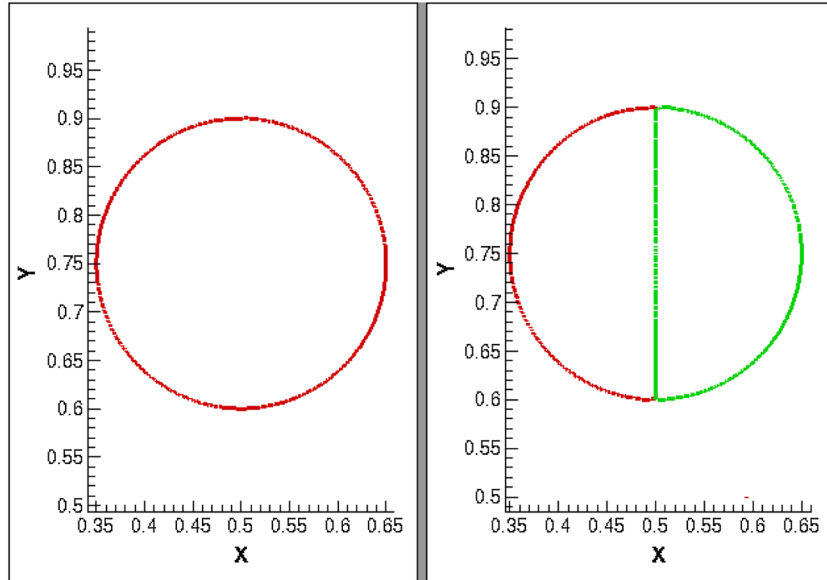


Figure 16. Deformation problem with period  $T = 8$ . Results at  $t = 8.0$ . Left: two materials. Right: three materials. The corresponding piecewise linear reconstructed interface is plotted. Base grid  $64 \times 64$ . Three levels of adaptive mesh refinement; effective fine-grid resolution  $512 \times 512$ .

#### 4.2. Three-dimensional reversible vortex

In this test problem, a sphere with radius 0.15 and center  $(0.35, 0.35, 0.35)$  is placed in the following flow field:

$$u = 2 \cos(\pi t / 3) \sin^2(\pi x) \sin(2\pi y) \sin(2\pi z) \quad (62)$$

$$v = -\cos(\pi t / 3) \sin^2(\pi y) \sin(2\pi x) \sin(2\pi z) \quad (63)$$

$$w = -\cos(\pi t/3) \sin^2(\pi z) \sin(2\pi x) \sin(2\pi y) \quad (64)$$

The initial sphere undergoes severe deformation for  $0 < t < 3/2$ . For  $3/2 < t < 3$ , the flow is ‘reversed’, and the final expected shape is a sphere again.

In Table II, we compare the error at  $t = 3$ ,  $E_{sym}$  (Equation (59)), for the following two cases: (i) Weymouth and Yue advection strategy [22] in which the initial sphere is artificially cut in half along the vertical axis and (ii) alternating EI–LE–EI advection strategy [20, 43] also in which the initial sphere is artificially cut in half along the vertical axis.

The results using the alternating EI–LE–EI advection strategy on a  $64 \times 64 \times 64$  grid are illustrated in Figures 17 and 18. For comparison purposes we also show the results for the deformation of the sphere in which the initial sphere is not artificially cut in half.

#### 4.3. Two-dimensional droplet on a slope

As in [44, 54], we tested our MOF algorithm by performing a convergence study for the relaxation of a 2D water droplet in gas on an  $18^\circ$  inclined solid plane. See Figure 19. There is no gravity. The inclined plane is defined as

$$\Omega_{plane} = \{(x, y) | \tan(18^\circ)(x - 3) + 1 - y > 0\} \quad (65)$$

The initial droplet is prescribed so that the initial contact angle is  $90^\circ$ . The initial droplet shape is defined as

$$\Omega_{drop} = \{(x, y) | 1 - ((x - 3)^2 + (y - 1)^2) > 0\} \cap \Omega_{plane}^C \quad (66)$$

Table II. Symmetric difference error from Section 4.2, for the reversible three-dimensional vortex.

Size	Three-material Weymouth and Yue	Three-material EI–LE–EI	Two-material EI–LE–EI
32	6.5E–3	5.6E–3	4.7E–3
64	2.1E–3	1.8E–3	2.0E–3

Errors are taken at the end time  $t = 3$ .  
EI, Eulerian implicit; LE, Lagrangian explicit.

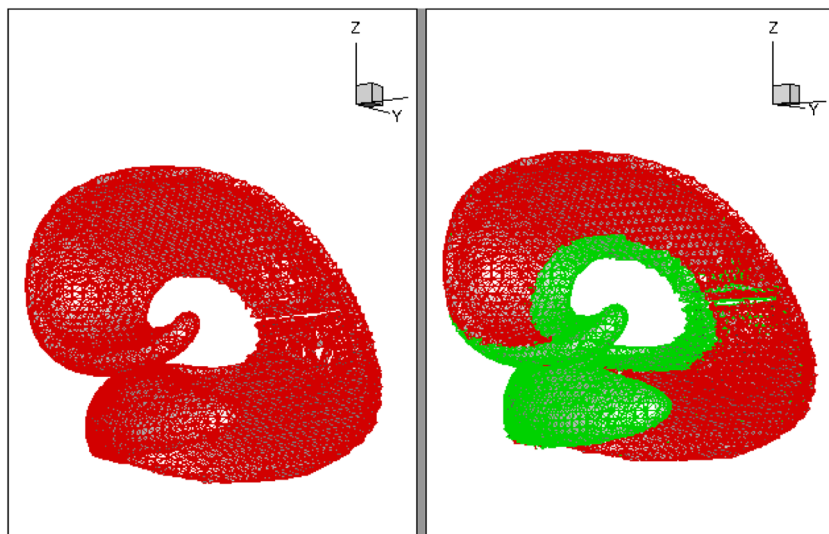


Figure 17. Three-dimensional deformation problem with period  $T = 3$ . Results at  $t = 1.5$ . Left: two materials. Right: three materials. The corresponding piecewise planar reconstructed interface is plotted.  $64 \times 64 \times 64$  grid.

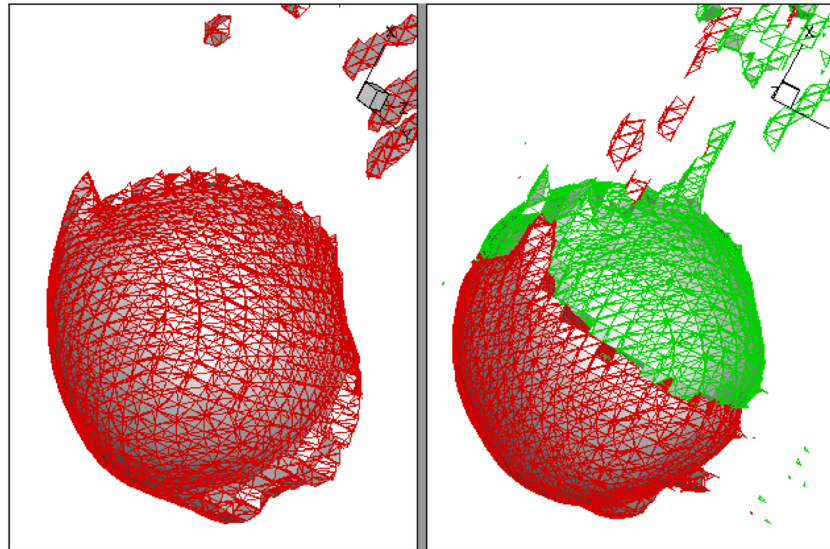


Figure 18. Three-dimensional deformation problem with period  $T = 3$ . Results at  $t = 3.0$ . Left: two materials. Right: three materials. The corresponding piecewise planar reconstructed interface is plotted.  $64 \times 64 \times 64$  grid.

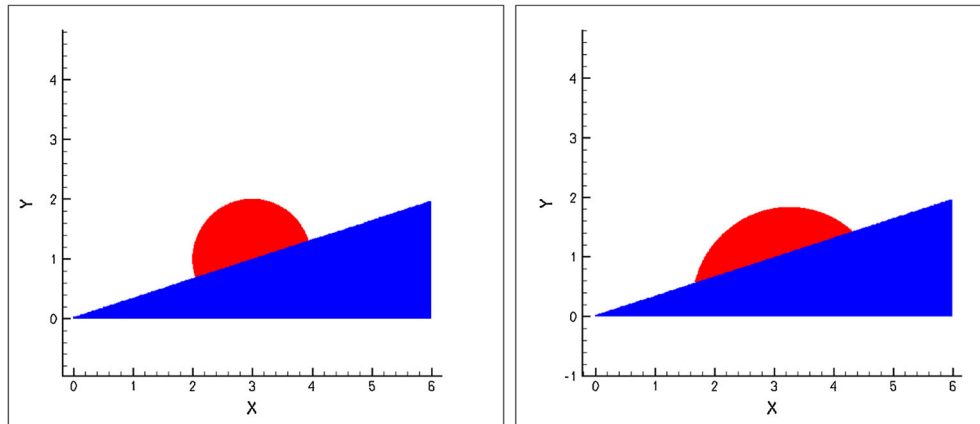


Figure 19. Relaxation of droplet (red) on a slope (blue) from a  $90^\circ$  contact angle to a  $60^\circ$  contact angle. Base coarse grid is a rectangular  $96 \times 48$  grid. Effective fine-grid resolution is  $384 \times 192$ . Left: initial conditions. Right: droplet at final static shape  $t = 0.8$ .

The dimensionless parameters are  $\rho_1 = 1$ ,  $\rho_2 = 0.0013$ ,  $\mu_1 = 0.16$ ,  $\mu_2 = 0.0025$ ,  $\sigma_{12} = 1118.0$ ,  $\sigma_{13} = 559.0$ , and  $\sigma_{23} = 1118.0$ . These parameters are nondimensionalized by the initial droplet radius  $r_0 = 0.06348$  cm (Figure 19) and a characteristic velocity  $U = 1$  cm/s. Material 1 corresponds to water (red), 2 corresponds to air (white), and 3 corresponds to solid (blue). The values of  $\sigma_{ij}$  correspond to a contact angle of  $60^\circ$ .

The expected drop height is

$$e_0 = (1 + \cos(\pi - \theta))R_\theta \quad (67)$$

and the expected base length is

$$L_0 = 2 \sin(\pi - \theta)R_\theta \quad (68)$$

where  $R_\theta$  is the final radius

$$R_\theta = \sqrt{\frac{\pi}{2\theta - \sin(2\theta)}} R_0 \quad (69)$$

In Table III, we give the percent error for  $e_0$  and  $L_0$  when computed on successively refined grids.

#### 4.4. Liquid lens test problem

We repeat the liquid lens test problem as in [42] (section 4.4 of [42]). Initially, there are three materials with material 2 occupying a circle of diameter 0.3 in the center of the domain, material 1 occupying the remaining top half of the computational domain, and material 3 occupying the remaining bottom half of the computational domain. All three materials have the same unit density and share the same viscosity of 1/60. The surface tension coefficients between materials 1 and 2 and between materials 2 and 3 were set to  $\sigma_{12} = 2/45$  and  $\sigma_{23} = 2/45$ , respectively. We tested our algorithm for four different values of the surface tension between materials 1 and 3 ( $\sigma_{13}$ ):  $\sigma_{13} = 3/90, 4/90, 5/90$ , and  $6/90$ . The expected steady-state solution has material 2 being stretched into a lens shape with a major axis length of  $L_0^{\text{exact}} = 0.381, 0.416, 0.460$ , and  $0.522$  for the four cases of  $\sigma_{13}$ . In Figure 20, we illustrate the initial and steady-state interfaces that we compute using our multimaterial MOF method for the case when  $\sigma_{13} = 5/90$ . In Table IV, we give the percent error in the major axis length for the four different cases of  $\sigma_{13}$ . In all of our test cases, the volume fluctuated

Table III. Percent error for the relaxation of a water drop on a sloped incline from a  $90^\circ$  contact angle to a  $60^\circ$  contact angle.

Levels	$100 \frac{ e_0 - e_0^{\text{exact}} }{e_0^{\text{exact}}}$	$100 \frac{ L_0 - L_0^{\text{exact}} }{L_0^{\text{exact}}}$
1	3.4	4.0
2	0.9	1.4
3	0.4	0.3

The computational domain is  $6 \times 3$  in dimensionless units. The computational grid is a hierarchy of adaptive, dynamic, rectangular grids with a base coarse grid of  $96 \times 48$  grid cells. The error is checked for three different grid resolutions.

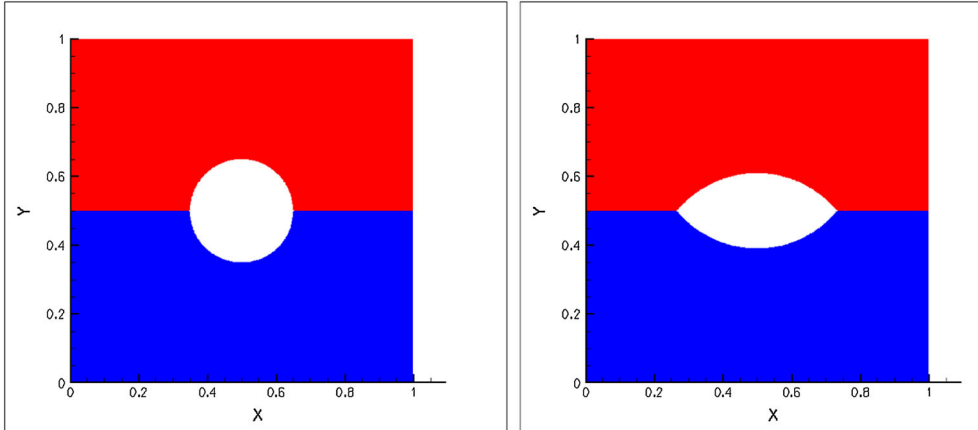


Figure 20. Stretching of a liquid lens. Red region indicates material 1, white region is material 2, and blue region is material 3. All materials have the same constant viscosity  $\mu = 1/60$ .  $\sigma_{12} = 2/45$ ,  $\sigma_{13} = 1/18$ , and  $\sigma_{23} = 2/45$ . The computational domain dimensions are  $1 \times 1$ . The base coarse grid is a rectangular  $64 \times 64$  grid. Effective fine-grid resolution is  $256 \times 256$ . Left: initial conditions. Right: liquid lens at  $t = 6$ .

Table IV. Percent error for the stretching of a liquid lens at static shape.

$\sigma_{13}$	$L_0$	$L_0^{\text{exact}}$	$100 \frac{ L_0 - L_0^{\text{exact}} }{L_0^{\text{exact}}} (\%)$
3/90	0.374	0.381	1.8
4/90	0.407	0.416	2.2
5/90	0.463	0.460	0.7
6/90	0.531	0.522	1.7

Initially, material 2 is a circle centered at  $(1/2, 1/2)$ , material 1 occupies the remaining top half, and material 3 occupies the remaining bottom half. The density and viscosity are constant for all three materials:  $\rho = 1$  and  $\mu = 1/60$ . The surface tension coefficients are  $\sigma_{12} = 2/45$ ,  $\sigma_{23} = 2/45$ , and  $\sigma_{13} = 3/90, 4/90, 5/90$ , and  $6/90$ . The computational domain dimensions are  $1 \times 1$ . The computational grid is a hierarchy of adaptive, dynamic, rectangular grids with a base coarse grid of  $64 \times 64$  grid cells and two levels of refinement.

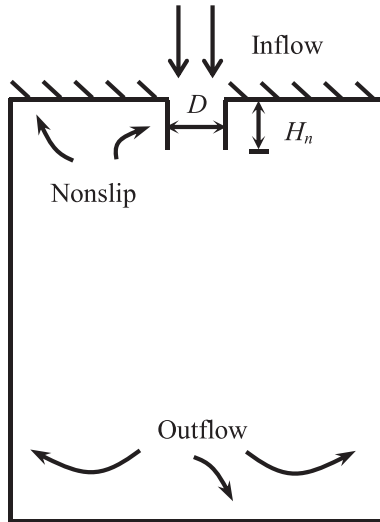


Figure 21. Illustration of nozzle geometry and computational domain for a downward jet.  $D$  is the nozzle diameter, and  $H_n$  is the nozzle height.

#### 4.5. Downward liquid jets

We study a downward liquid jet from a 3D round nozzle. Figure 21 illustrates the geometry of the nozzle and the computational conditions. The geometry of the nozzle can be defined by the nozzle diameter  $D$  and nozzle height  $H_n$ . Uniform flow velocity is assigned at the nozzle inlet. Nonslip boundary condition is applied at the nozzle walls and top surface. Outflow boundary condition is applied on the rest boundaries.

The following fluid properties are used: water density  $\rho_l = 1.0 \times 10^3 \text{ kg/m}^3$ , air density  $\rho_g = 1.225 \text{ kg/m}^3$ , water viscosity  $\mu_l = 1.3 \times 10^{-3} \text{ kg/m s}$ , air viscosity  $\mu_g = 2.0 \times 10^{-5} \text{ kg/m s}$ , surface tension  $\sigma = 7.28 \times 10^{-2} \text{ kg/s}^2$ , and the gravitational acceleration  $g = 9.8 \text{ m/s}^2$ .

In the simulation, the nozzle diameter  $D$  is 0.4 cm, and the nozzle height  $H_n$  is 0.6 cm. Two levels of AMR are used, resulting in a mesh that has 12 grid points per nozzle diameter.

When the flow rate is lower, jet behavior is dominated by the gravitational force and the surface tension force. Dripping regime will occur if the gravitational force is larger than the surface tension

force. Figure 22 shows the time evolution of the dripping regime at a low nozzle inlet velocity of  $v_0 = 6.0$  cm/s. When the flow rate is higher, the jet behavior is dominated by the inertial force and surface tension force, which leads to the jetting regime. Figure 23 shows the time evolution of the jetting regime at a high nozzle inlet velocity of  $v_0 = 20.0$  cm/s.

For the purpose of generality, we introduce three nondimensional parameters: the Reynolds number, the Weber number, and the Ohnesorge number. The Reynolds number,  $Re = \rho v_0 D / \mu$ , gives a measure of the ratio of inertial forces to viscous forces. The Weber number,  $We = \rho v_0^2 D / \sigma$ , represents the relative importance of inertia and surface tension. The Ohnesorge number,  $Oh = \sqrt{We}/Re = \mu/\sqrt{\rho\sigma D}$ , relates viscous forces to the inertial and surface tension forces.

For the studied high-inlet-velocity case, the Reynolds number is 307, the Weber number is 1.1, and the Ohnesorge number is 0.0034. The small Ohnesorge number means that the viscous forces are less important than the inertial force and surface tension. The breakup length, which is defined as the distance between the nozzle tip and the point just before the first drop of the liquid jet, can be

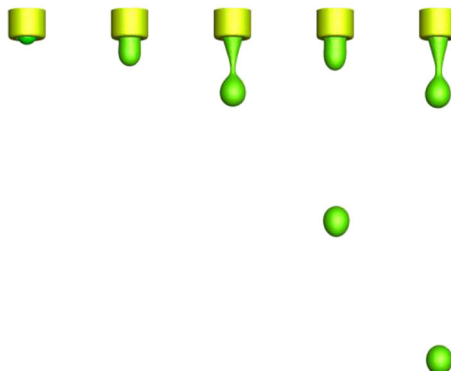


Figure 22. Snapshots of jet interface with a low velocity of  $v_0 = 6.0$  cm/s.

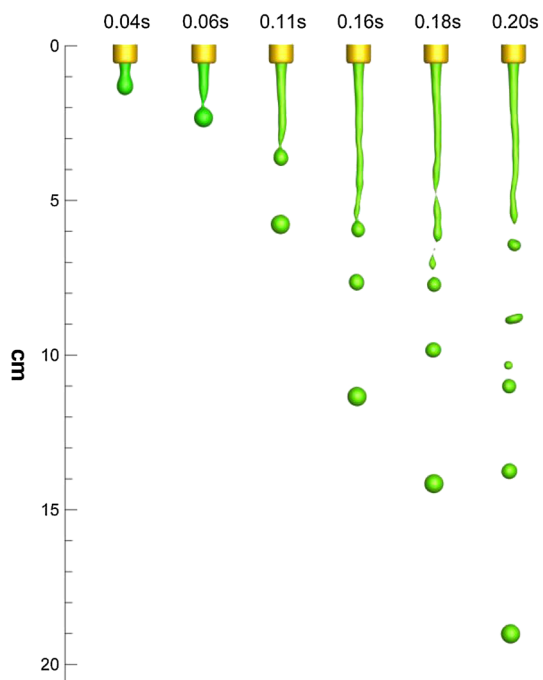


Figure 23. Snapshots of jet interface with a high velocity of  $v_0 = 20.0$  cm/s.

computed using the following formula [55]:

$$\frac{L}{D} = 1.04C \sqrt{We} \quad (70)$$

where  $L$  is the jet breakup length and  $C$  is an empirical parameter. Grant and Middleman [56] suggested the value of  $C = 13$  based on experimental data for a Rayleigh breakup of low-viscosity jets.

The computed breakup length, as shown in Figure 23, is about 6 cm, and it is very close to the value of 5.7 cm using equation (70).

#### 4.6. Upward liquid jets

We simulate upward liquid jet based on a geometry shown in Figure 24. In Figure 24,  $S_{UP}$  and  $S_{LOW}$  represent the lower and upper sections of the nozzle outlet, respectively. Two different nozzle configurations are used in our simulations. In the first case, both upper and lower surfaces are circles with the same diameter of 3.2 mm. In the second case, the lower surface is a circle, but the upper surface is an ellipse that has the same cross-sectional area as the lower surface, and the ratio of its major axis and minor axis is 3. The nozzle has an inlet diameter ( $D$ ) of 17.4 mm, a wall thickness  $H_1$  of 3 mm, and a height  $H_2$  of 9.4 mm. Three levels of AMR are used for these cases, and the effective grid size is about  $D_1/10$ , that is, 10 grid points per nozzle outlet diameter. The physical properties of the liquid and air are the same as that in the downward jet example.

In the first case, a uniform velocity of  $v_0 = 4.0$  cm is applied at the nozzle inlet. Figure 25 shows the jet interface evolution with time. The maximum jet height is 14 cm. The jet height first increases, reaches the maximum height, and then decreases with water accumulating at the jet tip because of the gravity effect.

In the second case, the same nozzle inlet velocity of 4.0 cm/s is applied. Figure 26 shows the jet interface evolution. It is noticed that after leaving the nozzle, the major axis and minor axis of the jet switch. This phenomenon was discussed by Lin [57] who argued that this switch is due to the effect of surface tension, which causes the jet section vibration about an equilibrium circle shape.

#### 4.7. Binary collisions of two water drops

Binary collisions of liquid drops have been experimentally studied in [58, 59] and numerically studied in [60–62]. For equal-sized head-on collisions, the outcomes depend on the Reynolds number and Weber number, which are defined as follows:

$$Re = \frac{\rho du}{\mu} \quad We = \frac{\rho du^2}{\sigma}$$

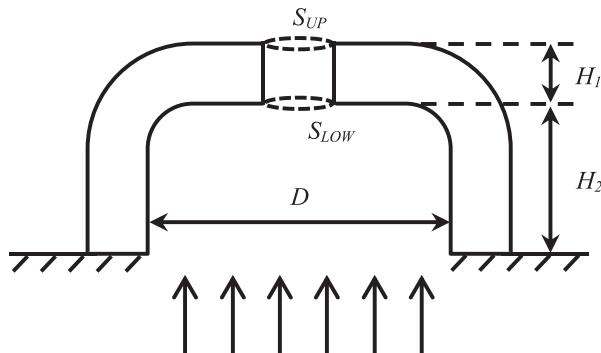


Figure 24. Illustration of nozzle geometry for upward jet.  $S_{UP}$  is the upper section of the nozzle outlet,  $S_{LOW}$  is the lower section of the nozzle outlet,  $D$  is the diameter of the nozzle inlet,  $H_1$  is the nozzle wall thickness, and  $H_2$  is the nozzle height.



Figure 25. Snapshots of upward liquid jet. A round nozzle is used.



Figure 26. Snapshots of upward liquid jet. The nozzle has a round low surface and an elliptical top surface.

where  $\rho$  and  $\mu$  are the liquid density and viscosity, respectively,  $d$  is the drop diameter,  $u$  is the relative velocity of the two drops, and  $\sigma$  is the liquid surface tension. With the Reynolds number in the range of 500 and 4000, Ashgriz and Poo found that the Reynolds number did not play a significant role on the outcome [58]. In Figure 27, we show results of the simulation of the head-on collision of two equal-sized water drops at the Weber numbers of 25, 40, and 96. In the experiments, it was found that reflexive separation occurs for a Weber number greater than 19 and coalescence or bouncing occurs for a Weber number less than 20. Our numerical results (Figure 27) corroborate these results.

#### 4.8. Binary collisions of one water drop and one diesel drop

In Figure 28, we show results of the collision of a diesel oil drop with a water drop. These results can be compared with the experimental results reported in [63]. As with the case for the collision of two water drops, again we have agreement between simulation and experiment for capturing the Weber number cutoff separating the coalescence regime from the reflexive separation regime.

#### 4.9. Impingement of droplet on a thin liquid film

The complex phenomenon of droplet impingement on a thin-film phenomenon is characterized by the Reynolds number  $Re$ , the Weber number  $We$ , the Ohnesorge number  $Oh$ , and the nondimensional film thickness  $H$  defined as follows:

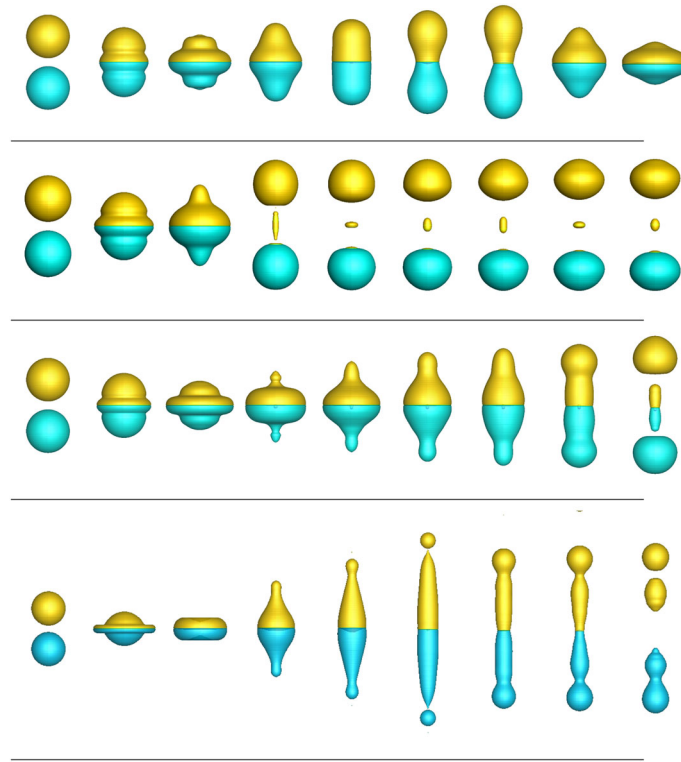


Figure 27. Numerical simulation of head-on collision of two water drops. From top to bottom, the Weber number is 15, 25, 40, and 96, respectively. The computational grid is a block-structured mesh with 16 cells per initial drop radius. One grid refinement is used (effective fine-grid resolution is 32 cells per initial drop radius). Results are in agreement with experiments [58]. We capture the correct transition point for reflexive separation.

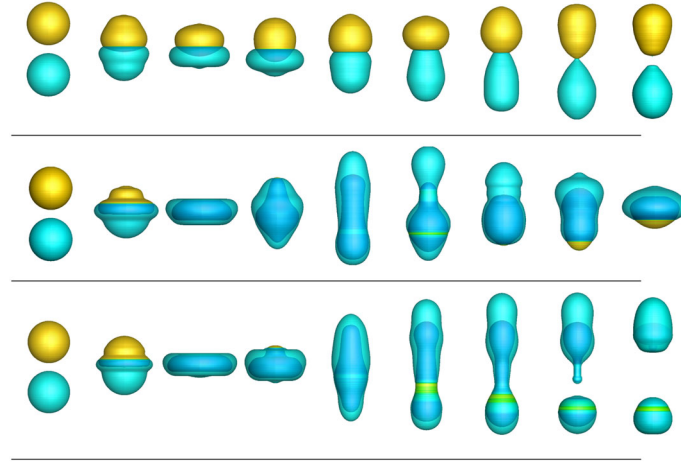


Figure 28. Numerical simulation of head-on collision of a diesel oil drop (cyan) with a water drop (gold) and resulting encapsulation. The Weber number equals 9.6, 45.3, and 58.9 for the top, middle, and bottom rows, respectively. Dimensionless drop diameter is 1, and computational domain size is  $0 < r < 1.3$  and  $-3.9 < z < 3.9$ . The computational grid is a block-structured dynamic adaptive mesh with  $48 \times 288$  coarse-grid cells and two additional levels of adaptivity (effective fine-grid resolution is  $192 \times 1152$ ). Results are in agreement with experiments [63]. We capture the correct transition point for reflexive separation.

Simulations are carried out in a three-dimensional axisymmetric ( $R-Z$ ) coordinate system.

$$\begin{aligned}
Re &= \rho v_0 D / \mu \\
We &= \rho v_0^2 D / \sigma \\
Oh &= \mu / \sqrt{\rho \sigma D} \\
H &= h/D
\end{aligned} \tag{71}$$

where  $v_0$  is the impact velocity,  $D$  is the droplet diameter, and  $h$  is the film thickness. Also, a nondimensional time  $T = t v_0 / D$  is introduced, and it is set to zero at the first contact between the droplet and the film.

At high  $We$  numbers, a crown structure is formed on the film surface, and liquid jets or secondary droplets are splashed from the crown rim. This is called the splashing regime. At low  $We$  numbers, the droplet may deposit on the film surface without secondary droplets. This is called the deposition regime. The critical  $We$  number separating the splashing regime and the deposition regime is studied by many researchers [64, 65]. Two Weber numbers are simulated:  $We = 100$ , which corresponds to the deposition regime, and  $We = 600$ , which corresponds to the splashing regime.

Figure 29 shows the time evolution of the deposition process, and Figure 30 shows the splashing process. The effective grid size is about  $D/70$  for the deposition case and  $D/135$  for the splashing case. Different from Rieber [66] who introduced random disturbance in his simulation, no random disturbance was introduced in our simulation. The initial distance from the droplet to the film is  $0.13D$ . For the deposition regime, as shown in Figure 29, a crown-like structure is formed at the first stage of the impact. This crown-like structure travels outwards with a maximum crown height of  $0.5D$  without any secondary droplet splashing. For the splashing regime, as shown in Figure 30, fingers are formed at the top of the crown rim. These fingers are then broken up into secondary droplets because of Rayleigh instability.

#### 4.10. Impingement of droplet onto a solid wall

The impingement of a droplet on a smooth solid wall can result in different regimes such as spreading, splashing, receding, and rebounding [67]. The Weber number, Ohnesorge number, and the contact angle play an important role in the impact dynamics. We choose the droplet diameter  $D = 3.6$  mm, density  $\rho = 1.0 \times 10^3$  kg/m<sup>3</sup>, viscosity  $\mu = 8.67 \times 10^{-4}$  kg/m s, surface tension  $\sigma = 7.17 \times 10^{-2}$  kg/s<sup>2</sup>, and impact velocity  $v_0 = 0.77$  m/s, which correspond to  $We = 30$  and

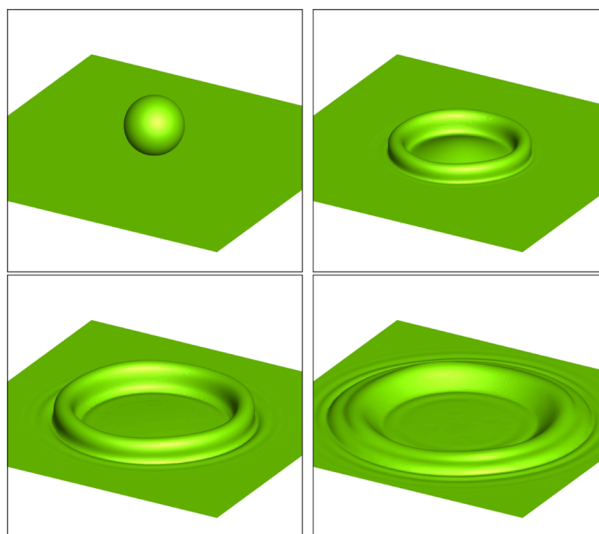


Figure 29. Snapshot of droplet–liquid film impingement,  $We = 100$ . From left to right, top to bottom:  $T = 0.0$ ,  $T = 1.0$ ,  $T = 2.0$ , and  $T = 3.0$ .

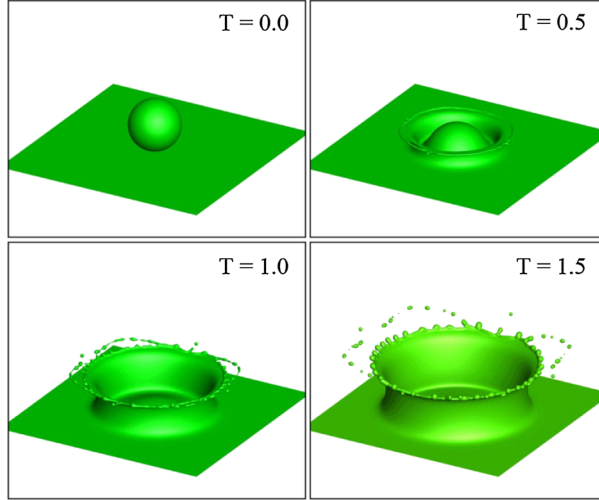


Figure 30. Snapshot of droplet–liquid film impingement,  $We = 600$ .

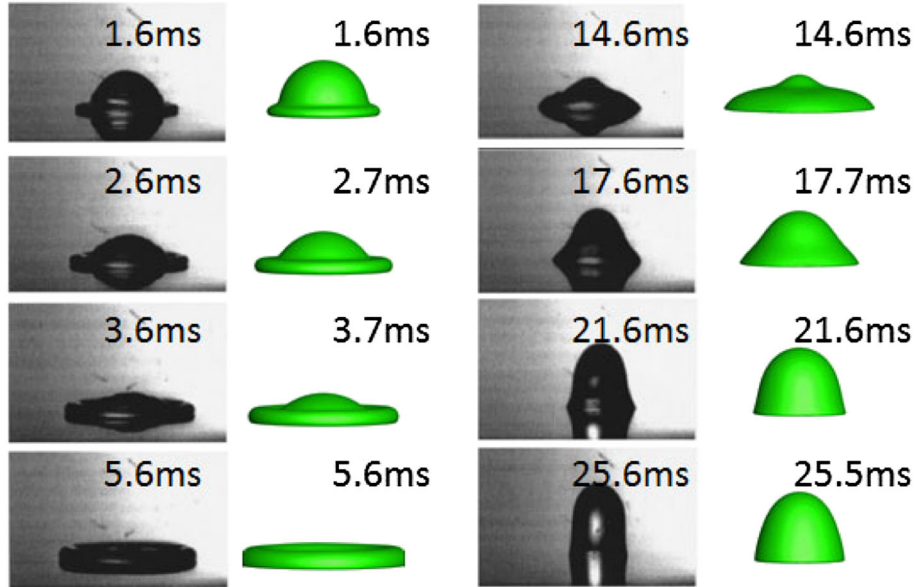


Figure 31. Droplet impinging on a solid wall. Left, experimental results from [69]. Right, present numerical results.

$Oh = 0.0017$ . A dynamic contact angle model from [68] is used, and the equilibrium contact angle is set to  $87^\circ$ . Two levels of grid adaptation are used, and the effective grid size is  $D/72$ .

Figure 31 shows the evolution of the droplet shape. The computed droplet shape is also compared with experimental data from Kim and Chun [69]. As can be seen from Figure 31, the experimental results and the numerical results are in good agreement.

## 5. CONCLUDING REMARKS

A new method was presented to study incompressible flows involving more than two materials. In this method, the MOF interface reconstruction method was used to capture the material interfaces. The directionally split CISL method was used to advect interfaces and momentum. The block-structured AMR was used to increase the resolution near material interfaces. Various 2D, 3D axisymmetric, and 3D problems were simulated. Comparisons were made with analytical or

experimental results. Our simulation showed that the proposed method is able to simulate multiphase problems involving more than two materials. The method is also able to capture the contact-line dynamics and triple junctions.

#### ACKNOWLEDGEMENTS

G. Li and Y. Lian acknowledge the support from General Electric. M. Sussman and M. Jemison acknowledge the support by the National Science Foundation under contract DMS 1016381. M. Arienti acknowledges the support by Sandia National Laboratories via the Laboratory Directed Research and Development program. Sandia National Laboratories is a multi-program laboratory managed and operated by Sandia Corporation, a wholly owned subsidiary of Lockheed Martin Corporation, for the U.S. Department of Energy's National Nuclear Security Administration under contract DE-AC04-94AL85000.

#### REFERENCES

1. Rayleigh L. On the instability of jets. *Proceedings of the London Mathematical Society* 1878; **10**:4–13.
2. Taylor G. Generation of Ripples by Wind Blowing Over Viscous Fluid. *The Scientific Papers of GI Taylor*, Vol. 3, Cambridge University Press, Cambridge, England, 1963; 244–254.
3. Sallam K, Dai Z, Faeth G. Drop formation at the surface of plane turbulent liquid jets in still gases. *International Journal of Multiphase Flow* 1999; **25**(6):1161–1180.
4. Sallam K, Aalburg C, Faeth G. Breakup of round nonturbulent liquid jets in gaseous crossflow. *AIAA Journal* 2004; **42**(12):2529–2540.
5. Palacios J, Gómez P, Zanzi C, López J, Hernández J. Experimental study on the splash/deposition limit in drop impact onto solid surfaces. *Proceedings of 23rd ILASS-2010*, Brno, Czech Republic, 2010; 1–7.
6. Raessi M. A level set based method for calculating flux densities in two-phase flows. *Annual Research Briefs*, Center for Turbulence Research, Stanford, 2008.
7. Raessi M, Pitsch H. Modeling interfacial flows characterized by large density ratios with the level set method. *Annual Research Brief*, Center for Turbulence Research, Stanford, 2009.
8. Brackbill J, Kothe DB, Zemach C. A continuum method for modeling surface tension. *Journal of Computational Physics* 1992; **100**(2):335–354.
9. Desjardins O, Moureau V, Pitsch H. An accurate conservative level set/ghost fluid method for simulating turbulent atomization. *Journal of Computational Physics* 2008; **227**(18):8395–8416.
10. Ménard T, Tanguy S, Berlemont A. Coupling level set/VOF/ghost fluid methods: validation and application to 3D simulation of the primary break-up of a liquid jet. *International Journal of Multiphase Flow* 2007; **33**(5):510–524.
11. Li X, Arienti M, Soteriou MC, Sussman M. Towards an efficient, high-fidelity methodology for liquid jet atomization computations. *AIAA Aerospace Sciences Meeting*, Orlando, FL, 2010; 4–7.
12. Hirt CW, Nichols BD. Volume of fluid (VOF) method for the dynamics of free boundaries. *Journal of Computational Physics* 1981; **39**(1):201–225.
13. Pilliod JE, Jr., Puckett EG. Second-order accurate volume-of-fluid algorithms for tracking material interfaces. *Journal of Computational Physics* 2004; **199**(2):465–502.
14. Osher S, Sethian JA. Fronts propagating with curvature-dependent speed: algorithms based on Hamilton–Jacobi formulations. *Journal of Computational Physics* 1988; **79**(1):12–49.
15. Sussman M, Smereka P, Osher S. A level set approach for computing solutions to incompressible two-phase flow. *Journal of Computational Physics*, Vol. 114.1, University of California, Los Angeles, 1994; 146–159.
16. Sussman M, Fatemi E, Smereka P, Osher S. An improved level set method for incompressible two-phase flows. *Computers & Fluids* 1998; **27**(5):663–680.
17. Sussman M, Almgren AS, Bell JB, Colella P, Howell LH, Welcome ML. An adaptive level set approach for incompressible two-phase flows. *Journal of Computational Physics* 1999; **148**(1):81–124.
18. Osher S, Fedkiw RP. Level set methods: an overview and some recent results. *Journal of Computational Physics* 2001; **169**(2):463–502.
19. Rudman M. A volume-tracking method for incompressible multifluid flows with large density variations. *International Journal for Numerical Methods in Fluids* 1998; **28**(2):357–378.
20. Scardovelli R, Zaleski S. Interface reconstruction with least-square fit and split Eulerian–Lagrangian advection. *International Journal for Numerical Methods in Fluids* 2003; **41**(3):251–274.
21. Jemison M, Loch E, Sussman M, Shashkov M, Arienti M, Ohta M, Wang Y. A coupled level set–moment of fluid method for incompressible two-phase flows. *Journal of Scientific Computing* 2013; **54**(2–3):454–491.
22. Weymouth GD, Yue DPK. Conservative volume-of-fluid method for free-surface simulations on Cartesian-grids. *Journal of Computational Physics* 2010; **229**(8):2853–2865.
23. Liovic P, Rudman M, Liow J-L, Lakehal D, Kothe D. A 3D unsplit-advection volume tracking algorithm with planarity-preserving interface reconstruction. *Computers & Fluids* 2006; **35**(10):1011–1032.
24. Chenadec VL, Pitsch H. A 3D unsplit forward/backward volume-of-fluid approach and coupling to the level set method. *Journal of Computational Physics* 2013; **233**(0):10–33.

25. Jemison M, Sussman M, Shashkov M. Filament capturing with the multimaterial moment-of-fluid method. *Journal of Computational Physics* 2015; **285**:149–172.
26. Sussman M, Puckett EG. A coupled level set and volume-of-fluid method for computing 3D and axisymmetric incompressible two-phase flows. *Journal of Computational Physics* 2000; **162**(2):301–337.
27. Son G, Hur N. A coupled level set and volume-of-fluid method for the buoyancy-driven motion of fluid particles. *Numerical Heat Transfer: Part B: Fundamentals* 2002; **42**(6):523–542.
28. Sussman M. A second order coupled level set and volume-of-fluid method for computing growth and collapse of vapor bubbles. *Journal of Computational Physics* 2003; **187**(1):110–136.
29. Wang Z, Yang J, Koo B, Stern F. A coupled level set and volume-of-fluid method for sharp interface simulation of plunging breaking waves. *International Journal of Multiphase Flow* 2009; **35**(3):227–246.
30. Dyadechko V, Shashkov M. Moment-of-fluid interface reconstruction. *Los Alamos Report LA-UR-05-7571*, Los Alamos National Laboratory, Los Alamos, New Mexico, 2005.
31. Ahn HT, Shashkov M. Multi-material interface reconstruction on generalized polyhedral meshes. *Journal of Computational Physics* 2007; **226**(2):2096–2132.
32. Dyadechko V, Shashkov M. Reconstruction of multi-material interfaces from moment data. *Journal of Computational Physics* 2008; **227**(11):5361–5384.
33. Ahn HT, Shashkov M. Adaptive moment-of-fluid method. *Journal of Computational Physics* 2009; **228**(8):2792–2821.
34. Ahn HT, Shashkov M, Christon MA. The moment-of-fluid method in action. *Communications in Numerical Methods in Engineering* 2009; **25**(10):1009–1018.
35. Jemison M, Sussman M, Arienti M. Compressible, multiphase semi-implicit method with moment of fluid interface representation. *Journal of Computational Physics* 2014; **279**:182–217.
36. Kucharik M, Garimella RV, Schofield SP, Shashkov MJ. A comparative study of interface reconstruction methods for multi-material ale simulations. *Journal of Computational Physics* 2010; **229**(7):2432–2452.
37. Wang Y, Simakhina S, Sussman M. A hybrid level set-volume constraint method for incompressible two-phase flow. *Journal of Computational Physics* 2012; **231**.19:6438–6471.
38. Sijoy CD, Chaturvedi S. Volume-of-fluid algorithm with different modified dynamic material ordering methods and their comparisons. *Journal of Computational Physics* 2010; **229**(10):3848–3863.
39. Schofield SP, Garimella RV, Francois MM, Loubere R. Material order-independent interface reconstruction using power diagrams. *International Journal for Numerical Methods in Fluids* 2008; **56**(6):643–659.
40. Caboussat A, Francois MM, Glowinski R, Kothe DB, Sicilian JM. A numerical method for interface reconstruction of triple points within a volume tracking algorithm. *Mathematical and Computer Modelling* 2008; **48**(11):1957–1971.
41. Schofield SP, Garimella RV, Francois MM, Loubere R. A second-order accurate material-order-independent interface reconstruction technique for multi-material flow simulations. *Journal of Computational Physics* 2009; **228**(3):731–745.
42. Kim J. Phase field computations for ternary fluid flows. *Computer Methods in Applied Mechanics and Engineering* 2007; **196**:4779–4788.
43. Aulisa E, Manservisi S, Scardovelli R, Zaleski S. Interface reconstruction with least-squares fit and split advection in three-dimensional Cartesian geometry. *Journal of Computational Physics* 2007; **225**(2):2301–2319.
44. Arienti M, Sussman M. An embedded level set method for sharp-interface multiphase simulations of diesel injectors. *International Journal of Multiphase Flow* 2014; **59**:1–14.
45. Stewart PA, Lay N, Sussman M, Ohta M. An improved sharp interface method for viscoelastic and viscous two-phase flows. *Journal of Scientific Computing* 2008; **35**(1):43–61.
46. Kang M, Fedkiw RP, Liu X-D. A boundary condition capturing method for multiphase incompressible flow. *Journal of Scientific Computing* 2000; **15**(3):323–360.
47. Sussman M, Ohta M. A stable and efficient method for treating surface tension in incompressible two-phase flow. *SIAM Journal of Scientific Computing* 2009; **31**(4):2447–2471.
48. Kwatra N, Su J, Grétarsson JT, Fedkiw R. A method for avoiding the acoustic time step restriction in compressible flow. *Journal of Computational Physics* 2009; **228**(11):4146–4161.
49. Almgren AS, Bell JB, Szymczak WG. A numerical method for the incompressible Navier–Stokes equations based on an approximate projection. *SIAM Journal on Scientific Computing* 1996; **17**(2):358–369.
50. Chorin AJ. Numerical solution of the Navier–Stokes equations. *Journal of Computational Physics* 1968; **22**:745–762.
51. Bell JB, Colella P, Glaz HM. A second-order projection method for the incompressible Navier–Stokes equations. *Journal of Computational Physics* 1989; **85**(2):257–283.
52. Sussman M. A parallelized, adaptive algorithm for multiphase flows in general geometries. *Computers and Structures* 2005; **83**:435–444.
53. Duffy A, Kuhnle A, Sussman M. An improved variable density pressure projection solver for adaptive meshes, 2012. unpublished. (Available from: <http://www.math.fsu.edu/~sussman/MGAMR.pdf>).
54. Noel E, Berlemont A, Cousin J, Menard T. Application of the immersed boundary method to simulate flows inside and outside the nozzles. *12th Triennial International Conference on Liquid Atomization and Spray Systems*, ICLASS 2012, Heidelberg, Germany, September 2; 1–7.
55. Ashgriz N. *Handbook of Atomization and Sprays*. Springer: New York, 2011.
56. Grant RP, Middleman S. Newtonian jet stability. *AICHE Journal* 1966; **12**(4):669–678.
57. Lin S-P. *Breakup of Liquid Sheets and Jets*. Cambridge University Press: New York, 2003.

58. Ashgriz N, Poo JY. Coalescence and separation in binary collisions of droplets. *Journal of Fluid Mechanics* 1990; **221**:183–204.
59. Orme M. Experiments on droplet collisions, bounce, coalescence and disruption. *Progress in Energy and Combustion Science* 1997; **23**:65–79.
60. Tanguy S, Berlemont A. Application of a level set method for simulation of droplet collisions. *International Journal of Multiphase Flow* 2005; **31**(9):1015 –1035.
61. Chen X, Yang V. Thickness-based adaptive mesh refinement methods for multi-phase flow simulations with thin regions. *Journal of Computational Physics* 2014; **269**(0):22 –39.
62. Nikolopoulos N, Nikas K-S, Bergeles G. A numerical investigation of central binary collision of droplets. *Computers and Fluids* 2009; **38**(6):1191 –1202.
63. Chen R-H, Chen C-T. Collision between immiscible drops with large surface tension difference: diesel oil and water. *Experiments in Fluids* 2006; **41**:453–461.
64. Cossali GE, Coghe A, Marengo M. The impact of a single drop on a wetted solid surface. *Experiments in Fluids* 1997; **22**(6):463–472.
65. Okawa T, Shiraishi T, Mori T. Production of secondary drops during the single water drop impact onto a plane water surface. *Experiments in Fluids* 2006; **41**(6):965–974.
66. Rieber M, Frohn A. A numerical study on the mechanism of splashing. *International Journal of Heat and Fluid Flow* 1999; **20**(5):455–461.
67. Yarin A. Drop impact dynamics: splashing, spreading, receding, bouncing. *Annual Review of Fluid Mechanics* 2006; **38**:159–192.
68. Jiang T-S, Soo-Gun O, Slattery JC. Correlation for dynamic contact angle. *Journal of Colloid and Interface Science* 1979; **69**(1):74–77.
69. Kim H-Y, Chun J-H. The recoiling of liquid droplets upon collision with solid surfaces. *Physics of Fluids* 2001; **13**:643.